CHAPTER 9

MICROSTRUCTURES of WORN DISCS

9.1 Introduction

Unlike many previous wear experiments, including the renowned work of Welsh[1965], the use of air cooling during these tests eliminated the effect of bulk heating as a test variable, i.e. the effect of thick oxide layers acting as a form of lubrication and/or the effect of bulk softening of near-surface structures (in ceasing to support such layers). This simulates part of the wear system for railway track where there is no bulk heating and debris falls away from the contact.

Under most conditions, wear performance was found to be controlled by the *directional* hardening characteristics of the pearlitic and bainitic microstructures described in Chapter 2. This hardening was generated by compressive stress from normal loading coupled with shear stress from the application of a unidirectional tangential force. The response of these altered structures to the wear mechanisms of adhesion, abrasion and micro-fatigue, plus their resistance to plastic deformation, determined the wear rates. Under certain severe conditions, fatigue on a larger scale was also found to be significant. Tribo-chemical wear, in this case the generation of thin oxide layers and debris due to surface heating on a microscopic, rather than macroscopic scale, was a feature of all tests irrespective of test loading and sliding conditions. Ductile inclusions were significant if their size, shape and distribution was such that they were flattened by the combined stresses to form planes of weakness. The volume fraction and distribution of brittle inclusions was too low in all the steels to be of significance. Microstructural differences were detected beneath the peaks and valleys of faceted discs. The difference in failure modes between "driven" (or "braking") and "driving" discs, described in Chapter 8, is further described and discussed.

All sections were examined by optical microscopy and a few by electron microscopy (SEM plus TEM carbon replicas). All were nickel plated prior to encapsulation to give edge retention (of the wear surface) during polishing. The nickel plate appears as a bright surface band on all the micrographs. Its hardness was around 300HV and it thus supported the wear surface for micro-hardness examinations. The etchant used was 2% Nital throughout.

9.2 Discs subject to pure rolling.

An Amsler test (Test 12) was carried out under conditions of pure rolling with a high maximum contact stress (p_o) of 1300 MPa (i.e. the discs are neither "braking" nor "driving"). After 50,000 bottom disc cycles neither disc had lost any weight. Both disc surfaces had a burnished, oxidised appearance and track edge deformation was very low compared to that seen on rolling-sliding tested discs at this contact stress. (Track width increase; 2.5% top disc, 1.8% bottom disc.) The coefficient of traction remained <0.01. (Coefficients for the rolling-sliding tests, given in Tables 8.1 and 8.2, ranged between 0.32 and 0.83.) Sections through both discs showed no matrix distortion in rolling direction.

A section through the top R52 disc is shown in Figure 9.1, no surface ratchetting is evident. Micro-hardness surveys of both sections showed that the work-hardening peak was sub-surface, as expected (cf. Chapter 3). It also showed that no hardening had occurred towards the surface (Figure 9.2).

(Note: all micro-hardness curves in this Chapter show, for each location, the average of at least 3 readings. Where disc wear surface hardness values are given, several impressions were taken on each disc; the ranges and average values are shown.)

9.3 The introduction of an element of sliding.

When, again at 1300 MPa p_o, an element of low slip or creepage was introduced, relatively heavy wear took place, with a high degree of surface distortion. (eg. Amsler Test 9 with 3% creepage $\{\gamma\}$.) Sections through the Test 9 R52 top driven disc and W64 bottom driving disc are shown in Figures 9.3 and 9.4, respectively. In both discs, the matrix had been strained to such a degree that ferrite areas and cementite lamellae within pearlite were near-parallel to the surface. The cementite lamellae had both fractured and plastically deformed in the process of alignment. (This feature is more clearly shown in the TEM micrographs discussed in Section 9.6.)

Ductile manganese sulphide (MnS) inclusions, which form "stringers" along the axis of rolled rail, and are hence normal to the plane of this section, had been "pancaked" flat and appear as deep etching lines in the R52 section. These became planes of weakness along which about one third of the surface flakes appeared to form. The orientation of MnS inclusions to the plane of the circumferential section through the bottom driving disc is less clear. Discs machined from a transverse "cheese" slice of W64 railway wheel tyre had slightly variable grainflows, thus the attitude and degree of "pancaking" of MnS "stringers" would be variable. The contact forces on the (W64) driving disc as it passes through the roll gap are such that, at these high contact stresses, thicker flakes were generated. These subsequently fractured off by a surface fatigue mechanism (Figure 9.4), with cracks propagating through a considerable thickness of the aligned matrix layers. The contact forces on the (R52) driven disc were such that flakes were thinned and retained on the wear surface for far more cycles. This difference in behaviour is discussed in Section 9.6.

The introduction of sliding increased the degree of track edge plastic distortion by an order of magnitude; around a 24% increase in track width spread in 20,000 cycles (see Table 6.3). Hardness profiles through these disc sections are given in Figure 9.5. The effect of the introduction of sliding on matrix hardening, at and near the wear surface, can be seen by comparing Figure 9.5 with Figure 9.2.

9.4 Microstructures of discs tested in the transitional (mild/severe) wear regime.

These sections were taken through discs tested at 900 MPa p_o and 3% γ. The wear results were given in Section 8.6.

R52/ W64 (Amsler Test 7)

Comparative wear curves are shown in Figure 8.17. The R52/W64 worn microstructures from Test 7 are shown in Figure 9.6 and the respective hardness curves in Figure 9.7. Comparing both figures with those for Test 9 (1300 MPa p_o, 3% γ; Figures 9.3, 9.4 and 9.5), it can be seen that matrix strain and work hardening were considerably reduced at this lower contact stress, as was track width spread (9.5%). Microstructural events, generated by matrix strain, appeared similar to those seen at the higher contact stress for the top driven R52 disc. They were also similar for the bottom driving disc with respect to cementite lamellae distortion, alignment and fracture, however surface flakes were thinner and fatigue fracture had taken place at flake tips, rather than through flake bodies, as seen at the higher contact stress. This difference was reflected in the W64 wear rate patterns for these two tests (cf. Tests 9 and 7, Figures 8.2 and 8.3).

B04/W64 (Amsler Test 16)

Circumferential sections through the B04 top driven disc and W64 bottom driving disc are shown in Figures 9.8 and 9.9, respectively. Microhardness curves are shown in Figure 9.10. The B04 disc hardened up to a similar near-surface value to the Test 7 R52 disc, however, as the initial bulk hardness was higher, the degree of work hardening was less. The wear rates of both discs were considerably higher than those of Test 7 (Figures 8.2 and 8.3), as was track width spread (Table 6.3). The B04 micrographs in Figure 9.8 indicate that thin flakes were rapidly formed and eroded away and that the near-surface structure was ratchetted in a similar manner to pearlite tested under these conditions. The MnS content of this steel was low and MnS inclusions appear to have had a minimal effect on the wear process. (This also applied to the other two bainitic steels.)

The hard (MA) phase particles in this bainite were sparser and far more regularly shaped than hard phase (cementite) lamellae in pearlite. They were re-aligned by matrix strain, but barely re-shaped or fractured; i.e. compared to pearlite, more soft ferrite phase would have been presented to the wear face. This, in turn, resulted in more adhesive wear and surface disruption of both discs (Figures 9.8 and 9.9). Disruption of lamellae alignment in the W64 disc reduced its wear resistance, hence its higher wear rate than the W64 disc of Test 7. However, even the semi-alignment of cementite lamellae kept the W64 disc wear rate below that of the B04 top disc.

B52/W64 (Amsler Test 14).

B52 steel has a mixed microstructure; a matrix consisting mostly of upper bainite with inter-lath carbide and smaller, less ductile areas of martensite and retained austenite containing coarse laths of lower bainite (which has finer, intra-lath carbide particles). These bulk structures were described in Section 2.8 and they are shown in Figures 2.16 to 2.18. These two types of structure had responded differently to tractive loading. Circumferential sections through the Test 14 B52 and W64 discs are shown in Figures 9.11 and 9.12, respectively. Microhardness curves are shown in Figure 9.13.

The upper bainitic areas accommodated more matrix strain than the martensite / lower bainitic areas. Under these test conditions, this resulted in wear surface cracks developing between the two structures (Figure 9.11). However, *no* material was observed to have spalled from the surface of any B52 disc; i.e. such cracks were retained. Only minor, isolated flakes formed on this B52 wear surface. The wear rate was extremely low (Figures 8.2 and 8.3). Near-surface hardening above bulk level was minimal (Figure 9.13).

The companion W64 disc had hardened up considerably compared with W64 discs from the other two tests. The pattern of near-surface matrix strain, and the formation of thick flakes which had fractured off well away from flake tips (Figure 9.12), was similar to that seen on the R52/W64 1300 MPa p_o test (Figure 9.4), but on a lesser scale. The frequency of these events must have been low as this was the lowest W64 wear rate under these conditions (Figures 8.2 and 8.3).

Faceted discs. (LEROS Tests 30 and 37)

The condition for these tests was also 900 MPa p_o and $3\%\gamma$. Test 30 wear rates were very similar to those of Test 7 (Figures 8.2 and 8.3). Circumferential sections were taken through peaks and troughs on the clearly faceted, R52 and B20 top "braking" discs from Tests 30 and 37, respectively.

Sections through a R52 peak and trough are shown in Figures 9.14 and 9.15, respectively. Microhardness surveys through these areas are shown in Figure 9.16*. (*Note: the X-axes, showing "distance beneath the surface" for surveys beneath each peak and trough, have been slightly offset to reflect the differential wear rates, i.e. hardness impressions for a given position are equidistant from the disc central axis.) Beneath both peak and trough, the mode of matrix strain appeared similar, although the peaks were smoother with fine flakes, whereas troughs had a more undulating, flake free surface. (Typical faceted discs are shown in Figures 7.14, 8.9b and 8.11.)

The degree of matrix strain, both visually and as determined by the hardness profile, differed beneath peaks and troughs, as did surface hardness. Note that hardness surveys were taken at mid-peak and mid-trough positions, whereas the highest degree of visual matrix strain was slightly towards the leading edge of the peaks. The near-surface matrix beneath the peaks was similar to that seen on the top Amsler disc of Test 7 (Figure 9.6), except that for the LEROS discs, it appeared to be more concentrated near the surface and the flakes were thinner. Cementite was fractured, deformed and aligned beneath wear surfaces of both peaks and troughs, however the degree of surface and near-surface strain was higher beneath peaks and surface flakes were generated. These results indicate that some form of "stick-slip" contact had taken place. These R52 facet microsections and respective hardness profiles can be compared to those of a corrugated pearlitic rail, shown in Figures 5.10c and 5.11c and d. A similar pattern is shown.

Matrix deformation features beneath the facets of the B20 top driven disc (Test 37) were similar to those of the faceted R52 disc section; with B20, MA phase and ferrite laths were more strain aligned beneath peaks compared to troughs. Structures beneath a B20 peak and trough are shown in Figures 9.17 and 9.18, respectively. Microhardness profiles are shown in Figure 9.19. Flaking was far finer on the peaks of this disc, compared to the R52 disc.

9.5 Microstructures of discs tested under severe conditions.

LEROS discs tested at high contact stress and low creepage (1800 MPa p_o, 1.5% γ)
As described in Chapter 8, Section 8.6, these test conditions resulted in a marked divergence of behaviour between top driven discs, irrespective of material, and bottom driving W64 discs (Figure 8.34). The top disc sliding wear rates were roughly equivalent to those seen at 900 Mpa p_o and 3% γ, whereas bottom disc wear rates were far higher (Figures 8.2 and 8.3). Also, only under these conditions did the ranking of top disc wear rates match that of respective material bulk hardness values (Tables 2.3). The R52, B20 and B52 surfaces were heavily flaked, (Figures 8.8 and 8.37) whereas few flakes were retained on the B04 surface (Figure 8.36).

All top discs and one bottom disc were sectioned. The R52 micro-structure, shown in Figure 9.20, was extensively ratchetted, with clear and deep alignment of fractured cementite lamellae and pancaked MnS stringers. Flake roots were as deep as 150μm and flake crack walls were undulating. This suggested that there had been a high rate of plastic flow of the flake material over the bulk (Figure 9.20b). The hardness profile is shown in Figure 9.21. This reflects the depth of matrix strain and work hardening shown in Figure 9.20, although if compared to Figure 9.5 for Test 9 (R52 at 1300 MPa p_o and 3% γ), it appears that the near-surface hardness was at an equivalent level and that the wear surface hardness was less at this higher contact stress. Perhaps the high plastic flow of the flakes was an additional mechanism, "feeding" the loss of flake tips whilst cementite lamellae alignment remained a protective mechanism.

Only these conditions of high contact stress and low creepage was the wear rate of B04 less than R52 (Figures 8.2, 8.3 and 8.34). Similarly, under moderately high contact stress (1300 MPa) and 3% creepage, it was slightly slightly less (Figures 8.2, 8.3, and 8.23). Under both test conditions, the appearance of the worn B04 discs differed from that of the other top "braking" disc materials, in that few large flakes adhered to the surface (Figure 8.36). However, large flakes were formed (from both top and bottom disc wear) and retained by the environment chamber exit air filter. For the 1800 MPa p_o condition, a 16mm circumferential microsection, taken through the worn B04 disc, contained only one sizeable flake plus occasional small flakes of a few microns depth. The matrix was extensively strained with deep alignment of hard MA phase particles (Figure 9.22). However, these particles were discrete with areas of strained ferrite between them. Perhaps flakes generated from such a structure were removed within one contact cycle of the rollers, however this would pre-suppose a high wear rate. (Figures 9.22b and c also clearly shows the difference in behaviour between ductile and brittle inclusions; Mns has been flattened whereas TiN has retained its shape and has thus initiated micro-cracks. However, it was felt that size and number of both types of inclusion were too low to make any significant contribution to the wear of these three bainitic steels.)

The hardness profile is shown in Figure 9.23. The degree and depth of work-hardening was markedly more than at 900 MPa p_o, 3% γ (Figure 9.10). This might help explain why B04 had a *lower* wear rate under this and another high contact stress conditions than at 900 MPa p_o and 3% γ (cf. Figures 8.2 and 8.3, Tests 16, 39 and 47). However, the depth and degree of work hardening of this B04 disc was less than that of the R52 disc similarly tested at 1800 MPa p_o and 1.5% γ (Figure 9.21), yet the R52 disc had a higher wear rate. This suggests that creepage and contact stress have different roles in amending the respective micro-structures to resist wear.

The B20 and B52 top driven discs similarly had low wear rates under these conditions of high contact stress and low creepage (Figures 8.2 and 8.3, Tests 48 and 49), although the B20 disc generated higher wear in the W64 bottom disc. As with R52, surface flakes were generated on both discs. The average flake crack depth was 104μm and 108μm for B20 and B52, respectively, compared to 42μm for R52. This suggests that, under these conditions, these bainitic steels were more resistant to flake tip loss than R52. A section through the B20 disc is shown in Figure 9.24. This shows that flakes had remained on the surface long enough for oxide to be formed in flake cracks. There was subsequent undulation of the crack walls as they moved with respect to each other; a similar situation to that seen in the R52 disc (Figure 9.20b). The distribution of hard MA phase within the near surface strain layer appeared similar to that seen in B04 (Figure 9.22), except that the volume content was far higher. The lath structure was completely broken down near the surface with compaction of hard phase particles.

The microhardness survey through the section is shown in Figure 9.25. The surface hardness level had been retained to a significant depth, whereas the level for the R52 and B04 discs dropped away (Figures 9.21 and 9.23). There had been overall hardening to about 0.5mm, less than that seen with R52 and B04 under these conditions, but markedly more than seen on the facet peaks of the B20 disc at half the contact stress (Figure 9.19). With both carbide free bainites, B04 and B20, perhaps only under these high contact stress conditions were the hard MA phase particles compacted enough to resist wear.

The B52 section is shown in Figure 9.26. Near-surface flaking features were similar to those seen for R52 and B20. Hardness survey results are shown in Figure 9.27. Sub-surface, the pattern is similar to B20, but surface hardening was slightly higher. The lath structure of the upper bainitic areas had been completely broken down by the high near-surface stresses, whereas the lower bainitic areas have been only partially, plastically deformed. Unlike the B04 disc tested under the same conditions (Figure 9.22), shear stresses in the matrix have been sufficient to fracture brittle TiN inclusions. In this instance, microcracks have linked the fractured particles (Figure 9.26d). Cracks were not observed to have formed between the upper and lower bainitic areas, as seen under milder test conditions (Figure 9.11).

Bottom W64 "driving" discs suffered severe wear under these test conditions, irrespective of the counter top disc material. Wear surface surveys indicated that a major wear mechanism had been low cycle fatigue fracture of thick flakes (Figures 8.38 and 8.39). Flake cracks propagated down to depths of 160μm, as shown in a section of the Test 48 W64 disc (Figure 9.28). There was some sub-surface crack initiation on, and along, pancaked MnS stringers and where propagation of steeply angles surface flake cracks reached such inclusions, thick plates of material had spalled off.

The micro-hardness scan of the Test 48 section is shown in Figure 9.25. Although the depth of hardening was high the comparative degree of near-surface hardening was not, cf. Figure 9.5. Perhaps the high wear rate slightly exceeded the rate at which hard phases were aligned and compacted within the structure, as seen under less severe test conditions. It was unfortunate that no time could be spared to test the bainitic structures as "driving" discs under these conditions, so as to gauge further the significance of this test variable.

LEROS discs tested at moderately high maximum contact stress and high creepage (1300 MPa p_o and 10% γ).

If test conditions are viewed as a product of maximum contact stress and creepage ($p_o\gamma$), these were the most severe conditions seen by *all* four rail steels. Rolling wear rates are schematically shown in Figure 8.4 and sliding wear rates in Figure 8.5. At these high creepages, there were significant differences between rolling wear rates and sliding wear rates, whereas such differences are minimal with the high contact stress, low creepage results previously described. At this high creepage, once again the carbide free structures, B04 and B20, had comparatively high wear rates, coupled with heavy wear of their respective bottom W64 "driving" discs (Figure 8.52).

Comparative microsections were taken through the bottom W64 discs of Test 42 (lower wear, against R52) and Test 44 (the highest wear rate, against B20). Possible wear mechanisms were discussed in Section 8.6, where it was suggested that different modes of surface "rippling" of each top driven disc might have induced differing degrees of surface (i.e. cementite alignment) disruption and local stress, thus affecting low cycle fatigue failure. The section though the lower wear rate Test 42 W64 disc is shown in Figure 9.29 and the section through the higher wear rate Test 44 W64 disc in Figure 9.30. The Test 44 disc appears to have been far more highly strained, with a greater degree of surface disruption and fatigue. This was reflected in the micro-hardness surveys (Figures 9.31 and 9.32 for Tests 42 and 44, respectively). The degree of sub-surface strain was higher in the Test 44 disc, but the surface hardness was lower, perhaps due to the greater disruption affecting the very near surface alignment of hard phases.

A section was taken through the top "braking" B20 disc (Test 44) tested under these conditions (Figure 9.33), for comparison with the B20 disc tested under the high stress, low creepage conditions described earlier (Figure 9.24, Test 48). Under the high creepage, low contact stress conditions (Test 44), the near surface, hard MA phase particles appeared to have been more plastically deformed. However, there are still discrete areas of ferrite, presented to the wear face, between the particles. Alignment of deformed particles has been disrupted by surface rippling. There were numerous small flakes generated on the ripples. The inclusions present, although low in volume, were also highly elongated, thus presenting some planes of weakness. The micro-hardness survey of the section is given in Figure 9.32. If compared to the Test 48 survey (Figure 9.25), the degree of sub-surface hardening was slightly less, as expected at a lower contact stress, but the degree of surface hardening was higher, perhaps reflecting the greater deformation and alignment of hard phases at this higher creepage. A mechanism that appears to favour the pearlitic structure, hence its comparatively low wear rate under these conditions, once surface disruption has been minimised.

Microstructures of Amsler discs tested at moderate maximum contact stress and high creepage (884 MPa p_o, 10% γ).

Wear results are presented schematically in Figures 8.4 and 8.5. With respect to the other severe wear results given previously in this section, it appears that at under these conditions, B04 became even more susceptible to high wear, whereas at this lower contact stress, wear rates for R52, B52 and W64 were reduced. The ranking of results was similar to that seen at 900 MPa p_o, 3% γ.

Wear surface microstructures of the top R52 and bottom W64 discs of Test 25 are shown in Figures 9.34 and 9.35; microhardness surveys are shown in Figure 9.36. The depth of strain hardening was shallow, with cementite lamellae alignment near to the surface. The rapid drop-off from a high worn surface hardness can be seen in Figure 9.36 for both top and bottom discs. Rolled-in debris appears to have partially disrupted near-surface, hard phase alignment in some areas of the bottom W64 disc (Figure 9.35), however this was not reflected in the hardness curve.

Wear surface microstructures of the top B04 and bottom W64 discs of Test 23 are shown in Figure 9.37 and 9.38; micro-hardness surveys are shown in Figure 9.39. Both wear surfaces were undulating and the sections reveal that this, and consequent high wear rates, were due to the abrasion and adhesion of compound debris. Although the sub-surface hardness of the B04 disc was slightly higher than the R52 disc, the worn surface hardness was lower.

Although the combined wear rate of the Test 22 (B52/W64) discs was similar to that of Test 25 (R52/W64), the latter W64 disc had a considerably higher wear rate. The wear surface microstructures of the top B52 and bottom W64 discs of Test 22 are shown in Figures 9.40 and 9.41, respectively; microhardness surveys are shown in Figure 9.42. There was some debris adhesion and consequent undulation of the B52 disc surface. The lower bainite areas had begun to deform plastically near the wear surface, whereas the upper bainite areas had deformed to a greater depth. There was considerable surface and sub-surface hardening of the matrix, more than that seen in the R52 and B04 discs. Although the W64 surface was relatively smooth, large flakes were generated; a different wear mechanism than that seen in the other two tests. The degree of W64 near-surface hardening was similar to that seen in the B04/W64 test (Test 23).

9.6 Electron microexamination of strained microstructures.

Some microsections were re-examined on a *scanning* electron microscope after deeper etching and gold flashing. The results did not add to the interpretations of the structures achieved through optical microscopy.

The microsections described in Sections 9.4 (Amsler tests at 900 MPa p_o, 3% γ) were chosen for further examination on two *transmission* electron microscopes (one at Leicester University and one at British Rail Research, Derby). Only limited results were achieved. Carbon replicas were successfully coated on the microsections but their removal without tearing proved difficult, due to adhesion to the (unetched) nickel plating. Once replicas had been peeled off, adherence of wear debris was a further problem, obscuring the structure within a few microns of the wear surfaces. Electron micrographs of the bulk structures of these steels are shown in Chapter 2.

TEM examination of R52.

Replicas of the near-surface structures of the R52 disc (Test 7) are shown in Figure 9.43. (Optical micrographs are shown in Figure 9.6.) Both show the progressive plastic deformation and fracture of cementite lamellae moving toward the wear surface and the alignment of short cementite lengths just below the wear surface. These lengths appeared to be "end-on", i.e. their flat faces were presented to the wear surface.

TEM examination of B04.

Replicas of the surface and near-surface structures of the B04 disc (Test 16) are shown in Figure 9.44. (Optical micrographs are shown in Figure 9.8.) Comparing these structures to the bulk structure shown in Figures 2.13 and 2.14, it can be seen that the lath structure has been completly broken down and that MA phase areas have, to a degree, both plastically deformed and aligned within the highly strained ferrite matrix.

TEM examination of B52.

A replica of the near-surface structure within the upper bainite region of the B52 disc (Test 14) is shown in Figure 9.45. (Optical micrographs are shown in Figure 9.11.) The more ductile, upper bainitic part of the B52 microstructure has been shown to change with most under traction induced strain. If this structure is compared to the bulk, upper bainitic structure (Figure 2.24) it can again be seen that the pattern of upper bainite laths, within a block, can no longer be recognised. The highly strained ferrite laths and inter-lath carbide have been partially aligned in the strain direction.

9.7 Summary

Pure rolling of discs, even under a high contact stress with no lubrication, generated no measurable wear and little strain alteration to the microstructures at, or near, the surface. Sub-surface hardening was marginal. Wear surfaces became burnished.

The introduction of a tangential force (under cooled, dry conditions) at the surface, albeit small, changed all these factors. Surface and near-surface microstructures were altered by the shear stresses generated. There was consequent work-hardening of matrix and plastic deformation at, and near, wear surfaces. Metallic flakes and protective oxide films were generated at the surfaces. These processes went through a running-in period; once steady state was achieved, wear rates stabilised. Where the wear rate was near a transition point, the wear pattern could suddenly change during a test to another steady state. Wear debris was generated by surface oxidation, adhesion, abrasion and by micro-fatigue fracture of metallic flake tips and surface oxide.

All the pearlite (R52 and W64) and bainite (B04, B20 and B52) microstructures examined were transformed by the shear stress generated by such rolling-sliding contact. The granular structures were broken down. All the structures work hardened in a directional manner and this increased wear resistance. As the severity of rolling load (i.e. contact stress) and sliding increased, disruption to this directional hardening could greatly increase the rate of wear.

Bolton et al[1982] and Bolton and Clayton[1984] attempted to catagorise such wear into three regimes, mild (I), severe (II) and catastrophic (III). To a certain degree, the results described here fall into these three catagories, although there are no sharp transitions. This will be more fully discussed in the next chapter.

The hardening mechanism of the structures was their compaction; i.e. the reduction of ferrite free space between hard phases such as cementite and MA phase. Such ferrite would become highly dislocated. Kalousek et al[1985] impressively demonstrated this effect in a study of pearlite, bainite and tempered martensite microstructures that were generated from selective heat-treatments of a single 0.72C CrMo rail steel. All structures were produced at three hardness levels and wear tested on a simulated rail-wheel contact rig under limited conditions. Their wear resistance ranking was generally that pearlite was superior to bainite, and that bainite was superior to tempered martensite. Careful TEM examination of these structures revealed the patterns of compaction with pearlite having the least ferrite free space and tempered martensite the most. As in the study described in this work, pearlite was initially softer, but under certain conditions it work hardened up to levels exceeding the other structures.

Under conditions of high contact stress and limited sliding, the comparative performance of the carbide-free bainitic steels greatly improved. No clear microstructural reason was detected. It was noticed throughout the tests that bainitic steel resistance to bulk plastic deformation (disc track "mushrooming") was far higher than with pearlite, even where their bainitic wear rates were far higher.

The W64 pearlitic bottom driving discs, nominally a similar steel to R52 top driven discs, behaved in a different manner under some conditions, particularly high contact stress. The angle of microstructural strain towards the surface was steeper and the thicker flakes generated would fracture near their root, rather than at the tips, with the consequent generation of surface pits. SEM studies suggested a mechanism of short cycle fatigue. This was most striking in the tests at 1800 MPa p_o and 1.5% γ. Another factor concerning W64 bottom discs was their high wear rate against all the bainitic steels.

The microstructural aspects of these results are further discussed in the following chapter.

9.8 References.

Bolton, P.J., Clayton, P. and McEwen, I.J. (1980). "Wear of rail and tyre steels under rolling-sliding conditions." *Proc. ASME/ASLE Lubrication Conf., San Francisco, USA, 18-21/08/80*. Pub. *ASLE Trans.* 25 (1), pp. 17-24.

Bolton, P.J. and Clayton, P. (1984). "Rolling-sliding wear damage in rail and tyre steels." *WEAR* 93, pp. 145-165.

Kalousek, J., Fegredo, D.M. and Laufer, E.E. (1985). "The wear resistance and worn metallurgy of pearlite, bainite and tempered martensite rail steel microstructures of high hardness." *WEAR* 105 (3) pp. 199-222.

Welsh, N.C. (1965). "The dry wear of steels (Parts I & II)". *Phil. Trans. Royal Soc.* 257 (A1077), pp. 31-70.

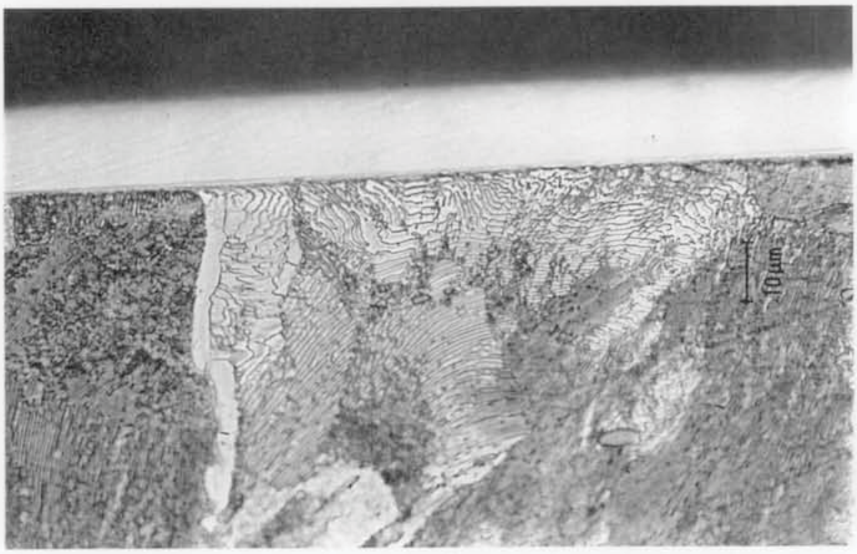

(x850 mag.)

Figure 9.1 Wear surface circumferential section through a R52 top disc, Amsler tested at 1300 MPa maximum contact stress, p_o, and *zero* creepage, γ, (i.e. pure rolling) for 50000 revolutions.

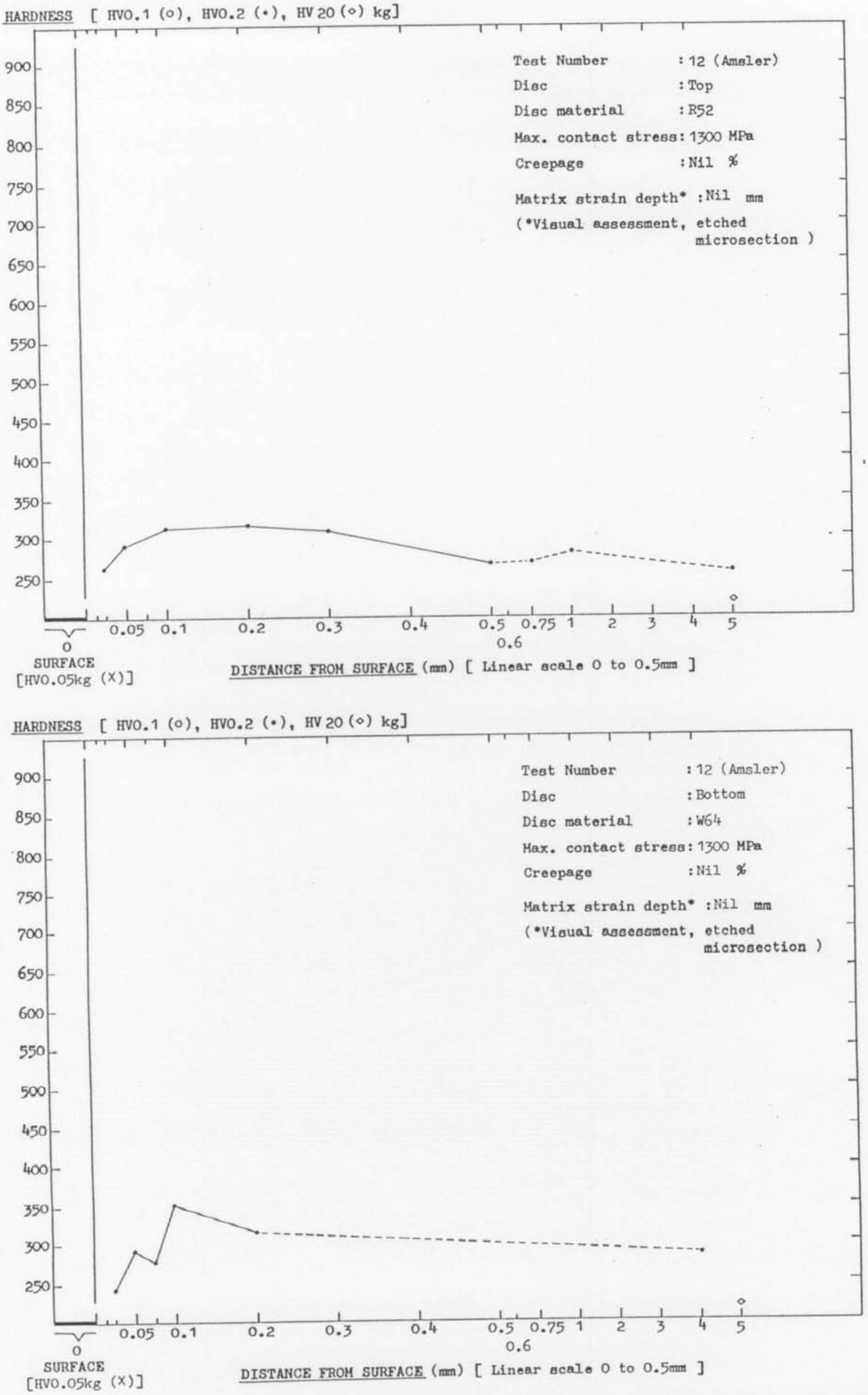

Figure 9.2 Microhardness profiles of wear surface circumferential sections from R52 top and W64 bottom discs, Amsler tested at 1300 MPa p_0 and *zero* γ (pure rolling) for 50000 revolutions.

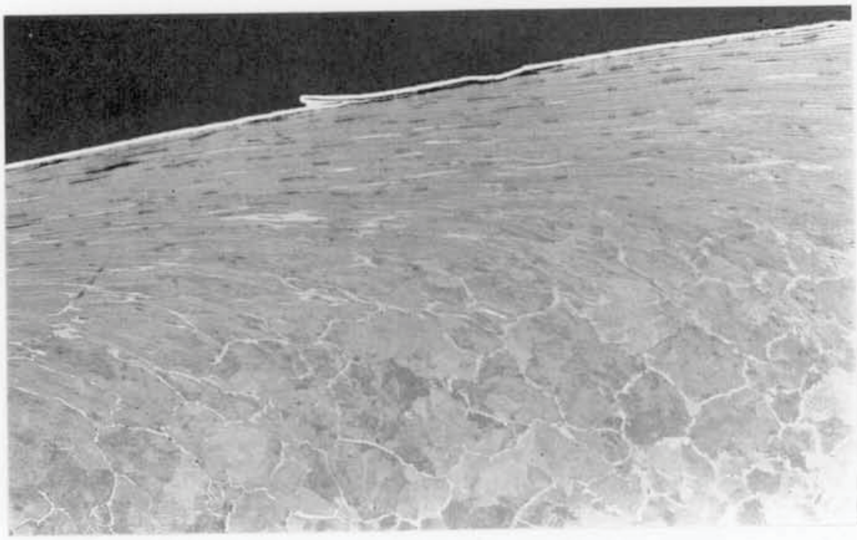

a
(x85 mag.)

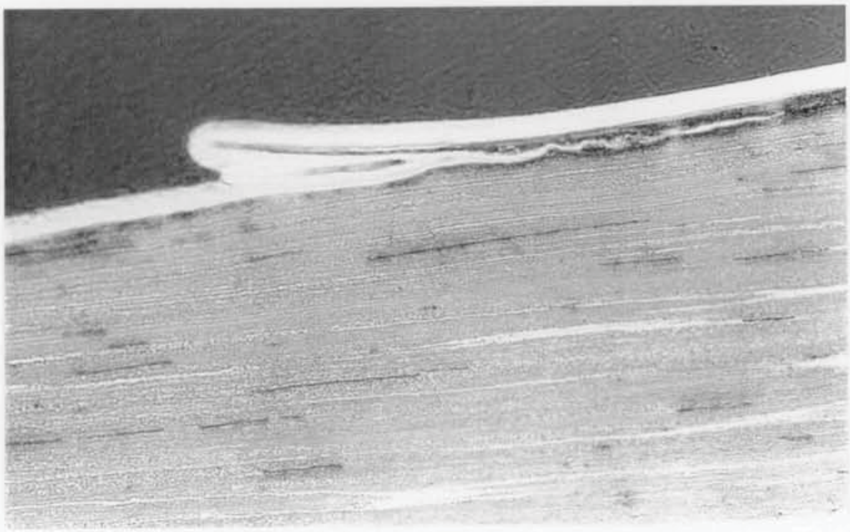

b
(x425 mag.)

Figure 9.3 Wear surface circumferential section through a R52 top driven (i.e. "braking") disc, Amsler tested at 1300 MPa p_o and 3% γ (Test 9).
(a) Overview showing "ratchetting" (i.e. cyclic, directional matrix strain) and surface flake. Wear by thin flake tip fracture.
(b) Near-parallel matrix strain at the surface and pancaked MnS inclusion stringer cross sections.

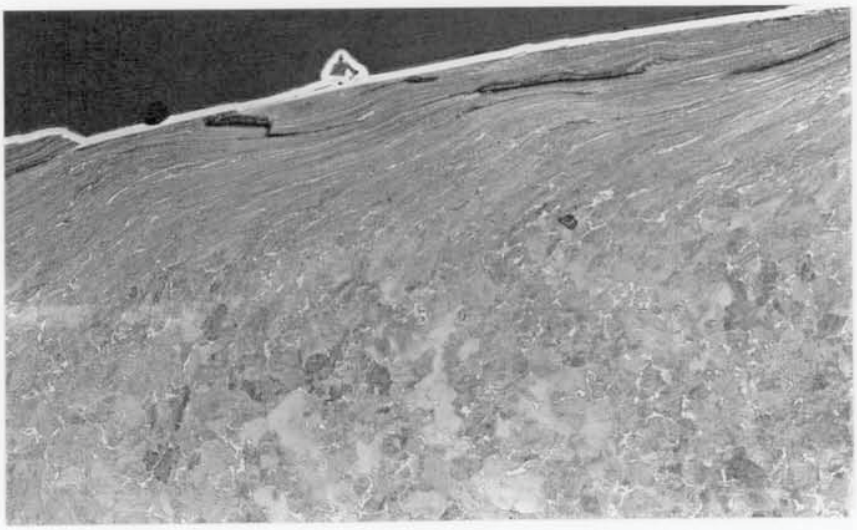

a
(x85 mag.)

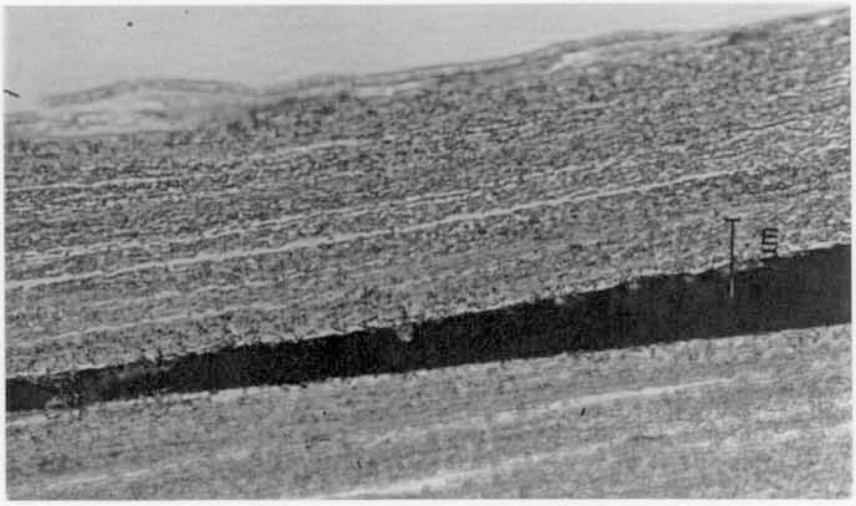

b
(x1063 mag.)

Figure 9.4 Wear surface circumferential section through a W64 bottom driving disc, Amsler tested against R52 at 1300 MPa p_o and 3% γ (Test 9). (a) Overview. For driving discs, typical fracture of flakes near their root. (b) Aligned structure within a flake.

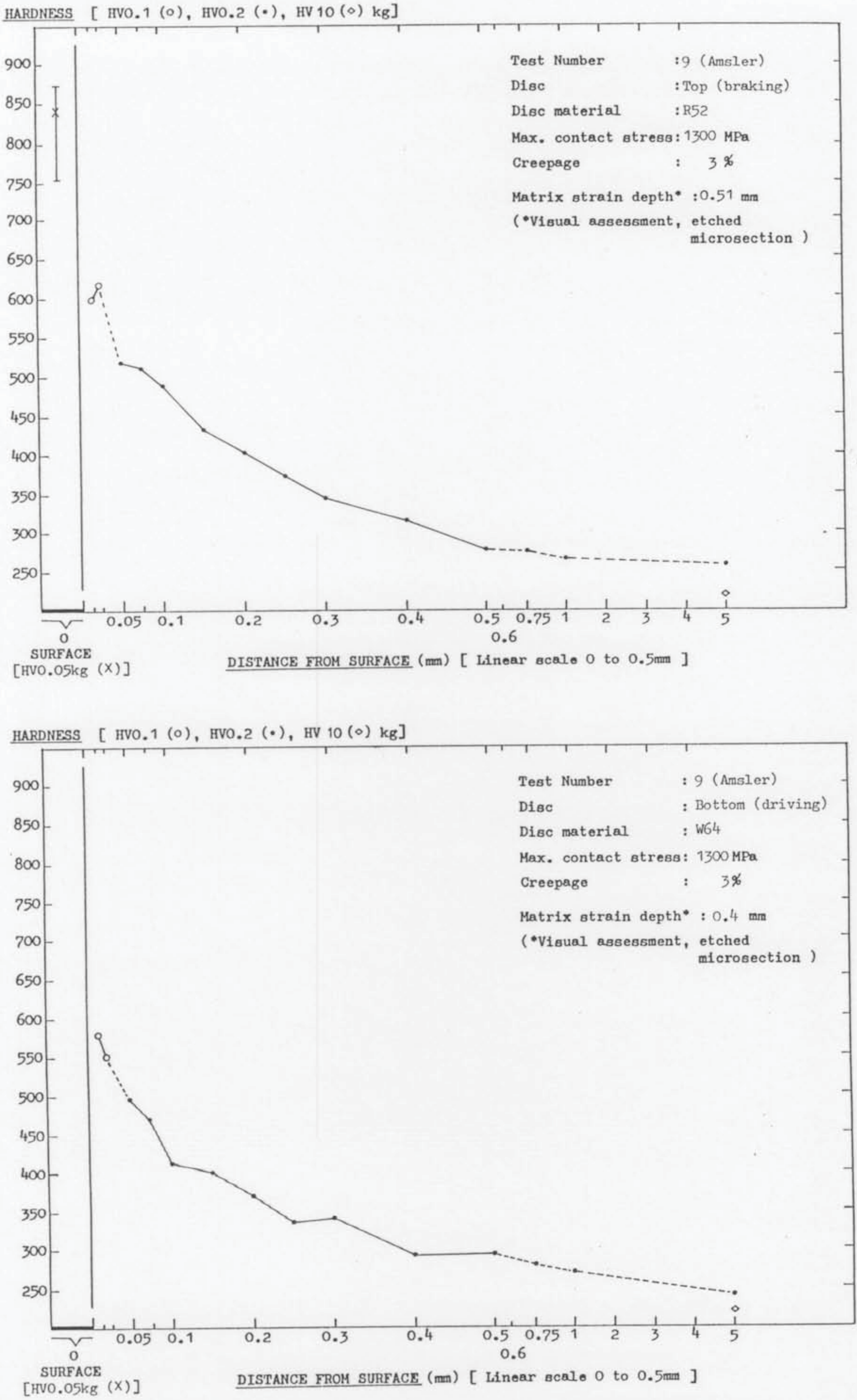

Figure 9.5 Microhardness profiles of the R52 top disc and W64 bottom disc wear surface circumferential sections shown in Figures 9.3 and 9.4, respectively.

a
(x170 mag.)

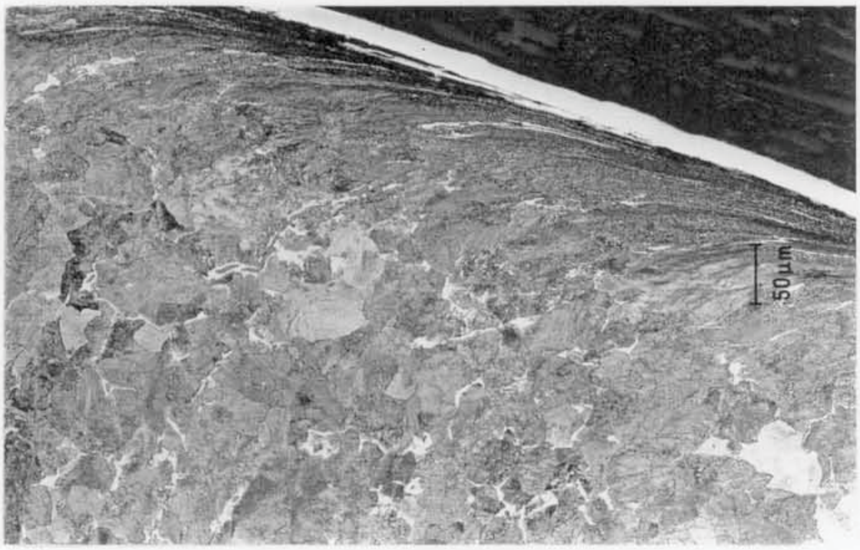

b
(x170 mag.)

Figure 9.6 Wear surface circumferential sections through (a) R52 top disc and (b) W64 bottom disc, Amsler tested at 900 MPa p_o and 3% γ (Test 7). Shallower ratchetting at this contact stress.

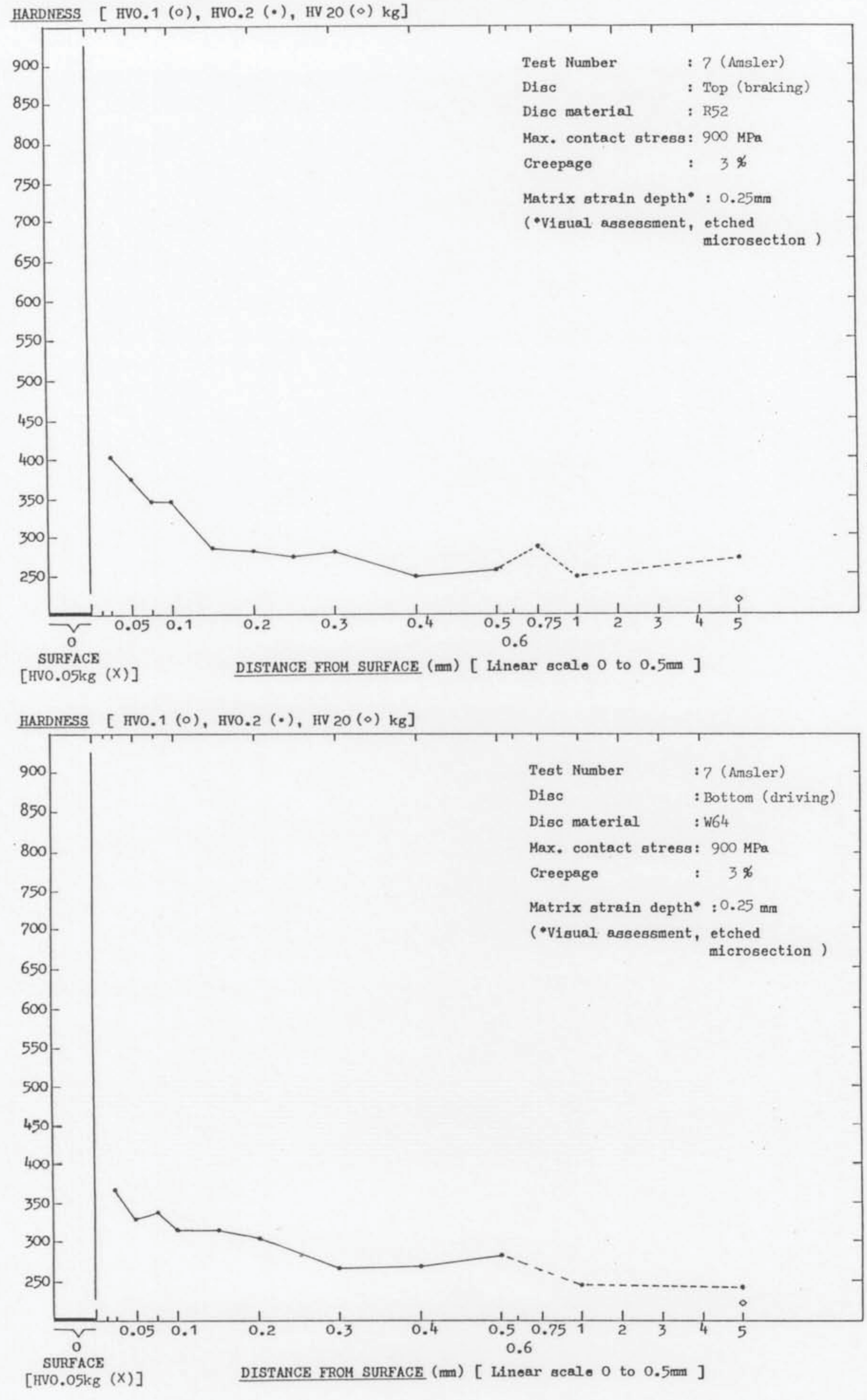

Figure 9.7 Microhardness profiles of the R52 top disc and W64 bottom disc wear surface circumferential sections shown in Figure 9.6.

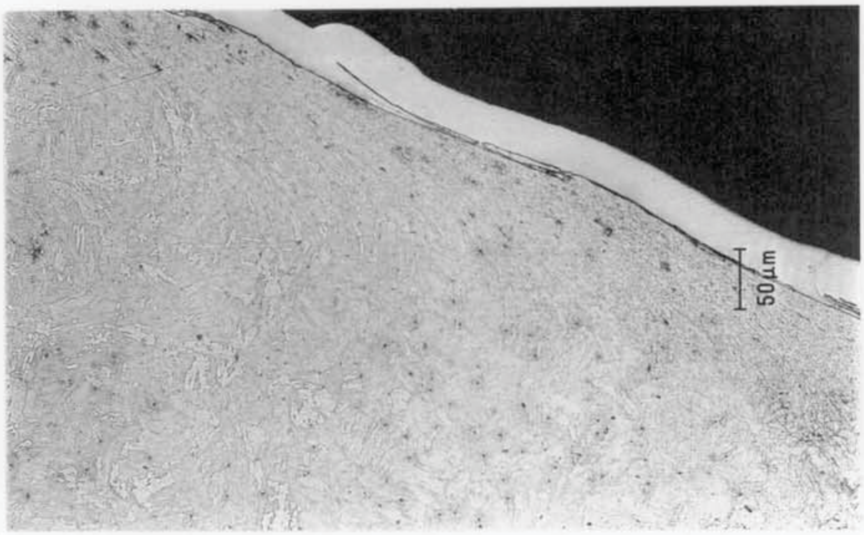

a
(x170 mag.)

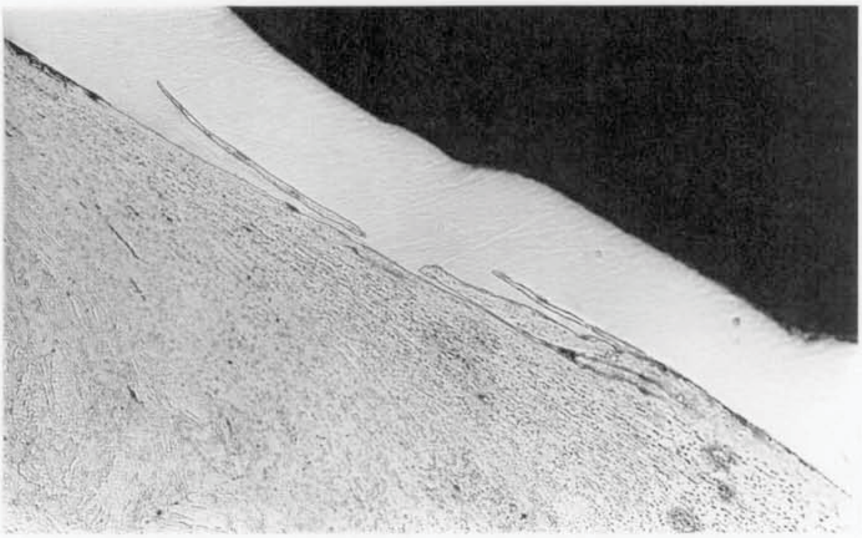

b
(x425 mag.)

Figure 9.8 Wear surface circumferential section through a B04 top driven disc, Amsler tested at 900 MPa p_o and 3% γ (Test 16).
(a) Overview showing ratchetting and surface flake.
(b) Shallow near-surface ratchetting; wear by thin flake tip fracture.

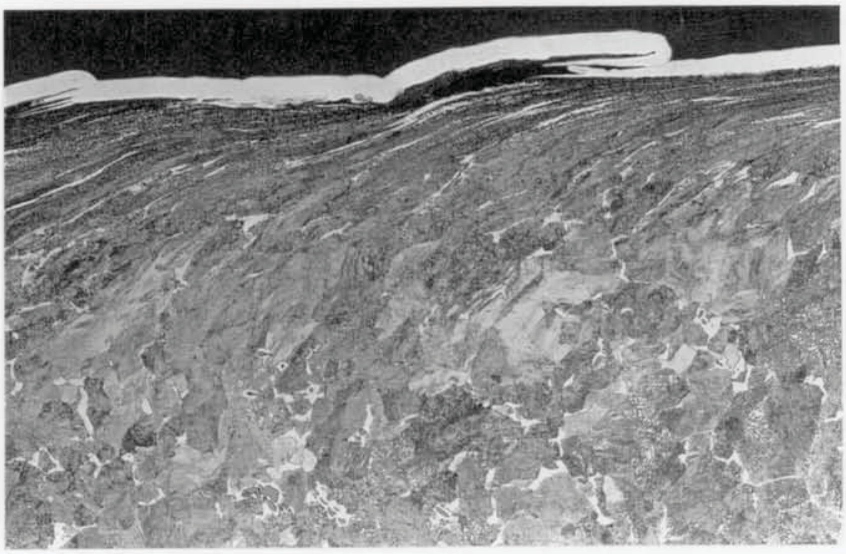

a
(x170 mag.)

b
(x425 mag.)

Figure 9.9 Wear surface circumferential section through a W64 bottom driving disc, Amsler tested against B04 at 900 MPa p_o and 3% γ (Test 16). The surface is more disrupted compared with the section shown in Figure 9.6b.

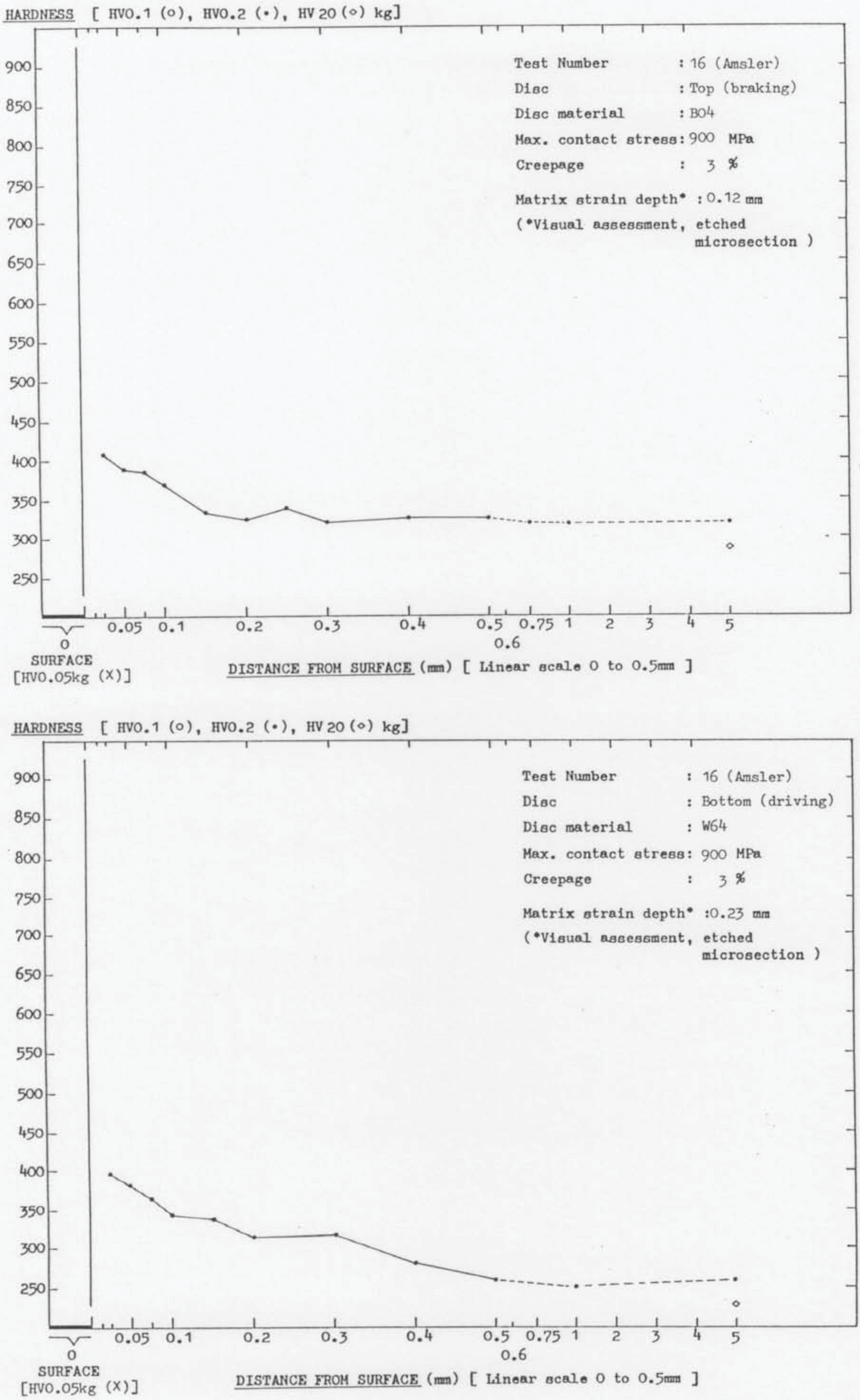

Figure 9.10 Microhardness profiles of the B04 top disc and W64 bottom disc wear surface circumferential sections shown in Figures 9.8 and 9.9.

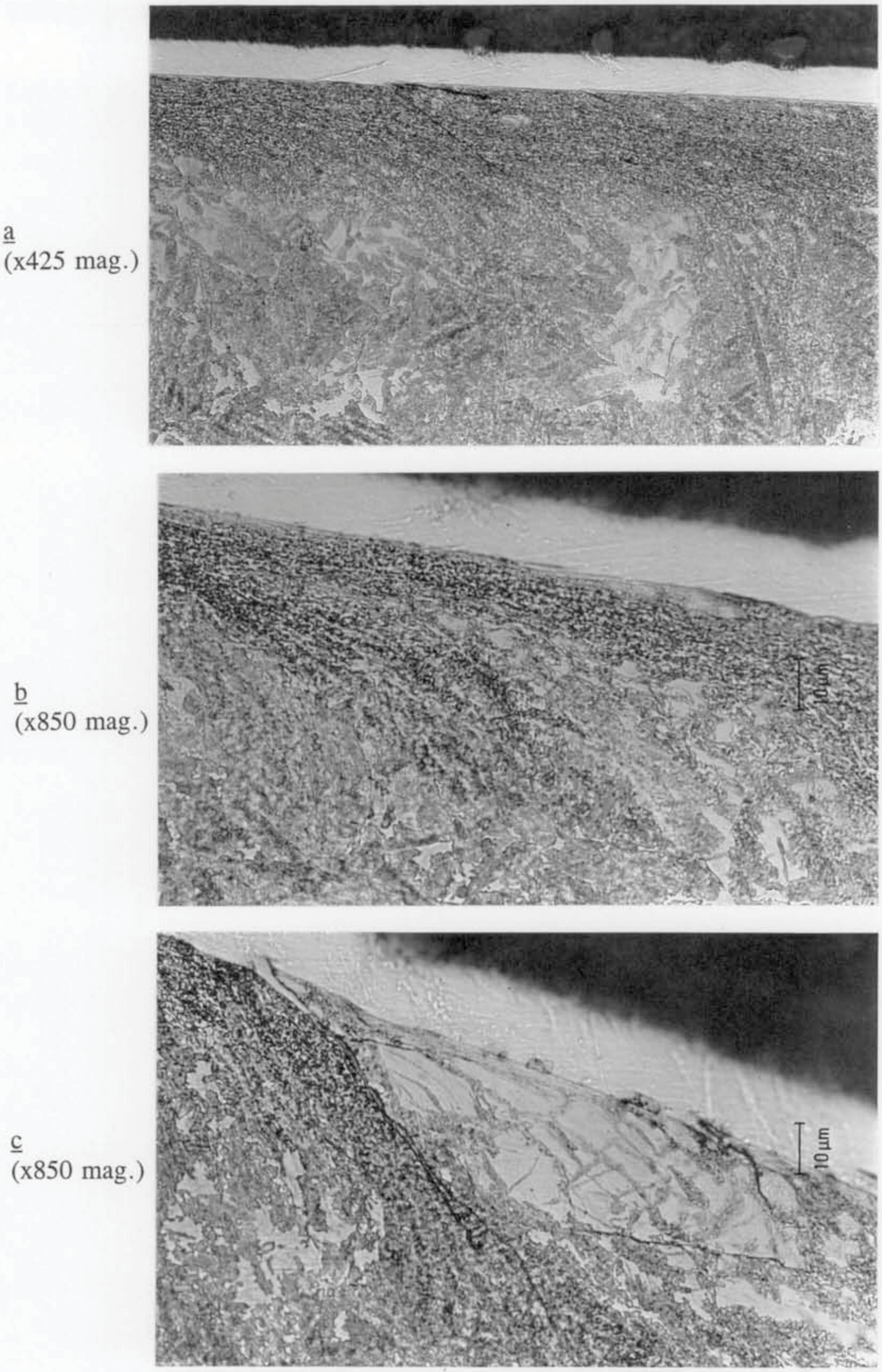

a (x425 mag.)

b (x850 mag.)

c (x850 mag.)

Figure 9.11 Wear surface circumferential section through a B52 top driven disc, Amsler tested at 900 MPa p_o and 3% γ (Test 14).
(a) Close view showing shallow ratchetting and fine surface fracture below a small flake.
(b) Detail, showing rigidity of lower bainite / martensite zones near the surface.
(c) Fracture between the strained upper bainite matrix and rigid lower bainite / martensite zone at the wear surface.

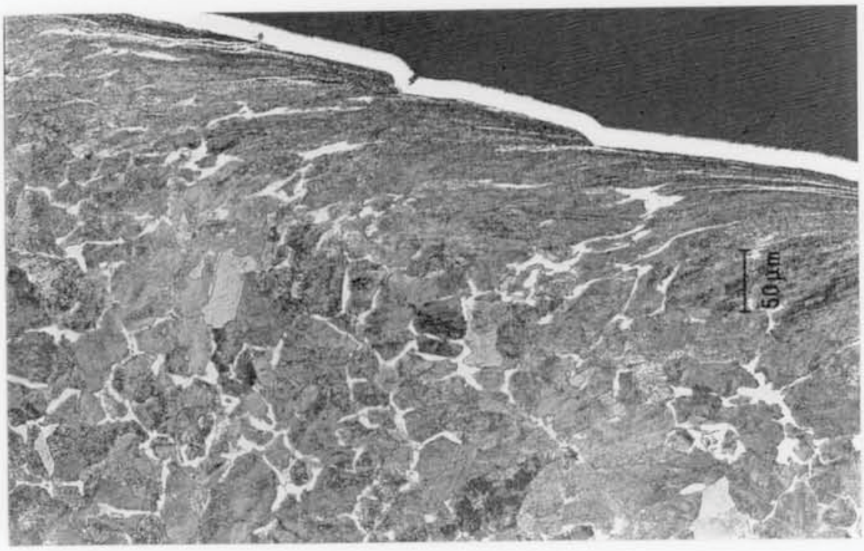

a
(x170 mag.)

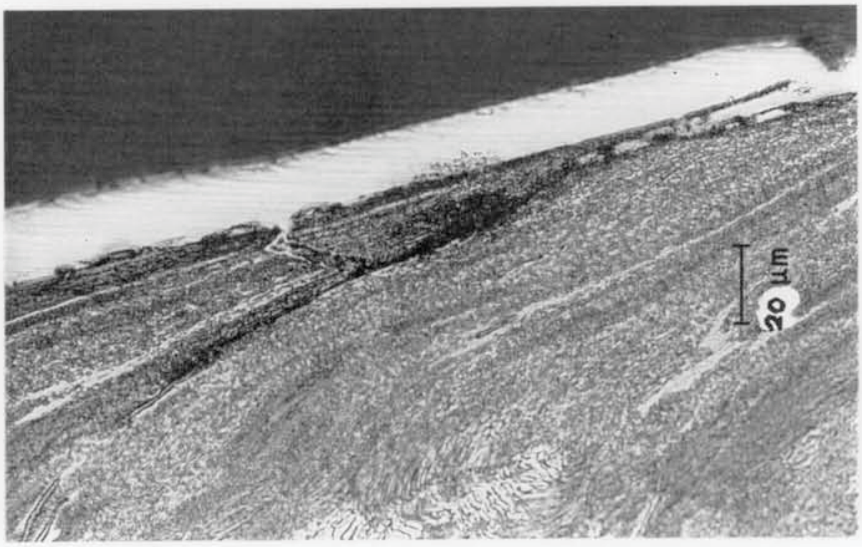

b
(x561 mag.)

Figure 9.12 Wear surface circumferential section through a W64 bottom driving disc, Amsler tested against B52 at 900 MPa p_o and 3% γ (Test 14). Undulating surface from block fracture of surface flakes.

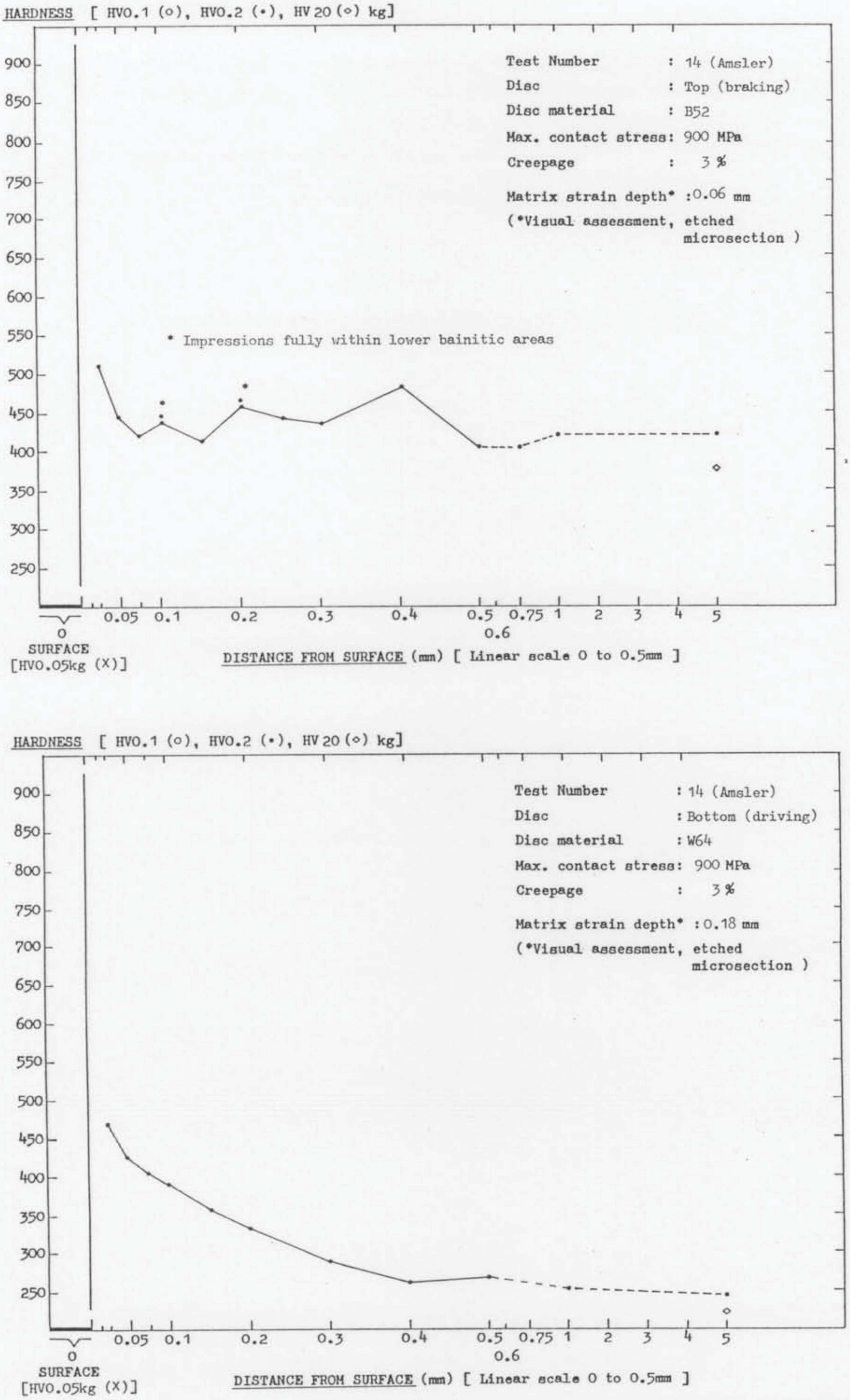

Figure 9.13 Microhardness profiles of the B52 top disc and W64 bottom disc wear surface circumferential sections shown in Figures 9.11 and 9.12. The hardness variation within the inhomogenous B52 structure is evident.

(X170 mag.)

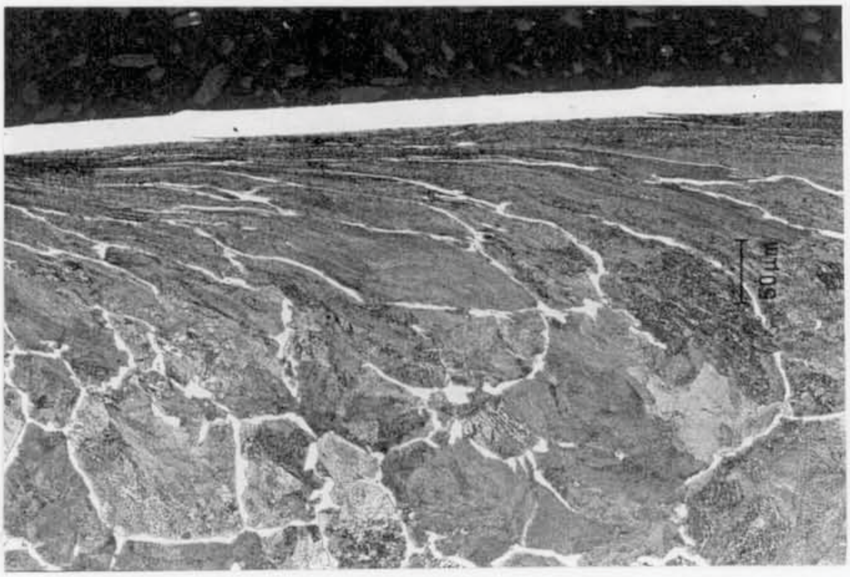

Figure 9.14 Wear surface circumferential section through a R52 top driven disc, LEROS tested at 900 MPa p_o and 3% γ (Test 30). *Section through a facet peak.*

(X170 mag.)

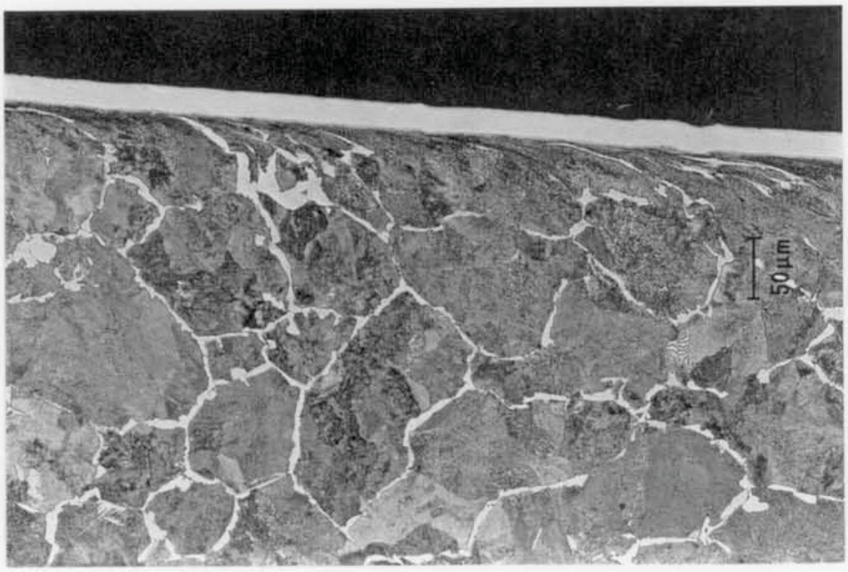

Figure 9.15 Wear surface circumferential section through a R52 top driven disc, LEROS tested at 900 MPa p_o and 3% g (Test 30). *Section through a facet trough.* Less ratchetting than seen on the facet peak.

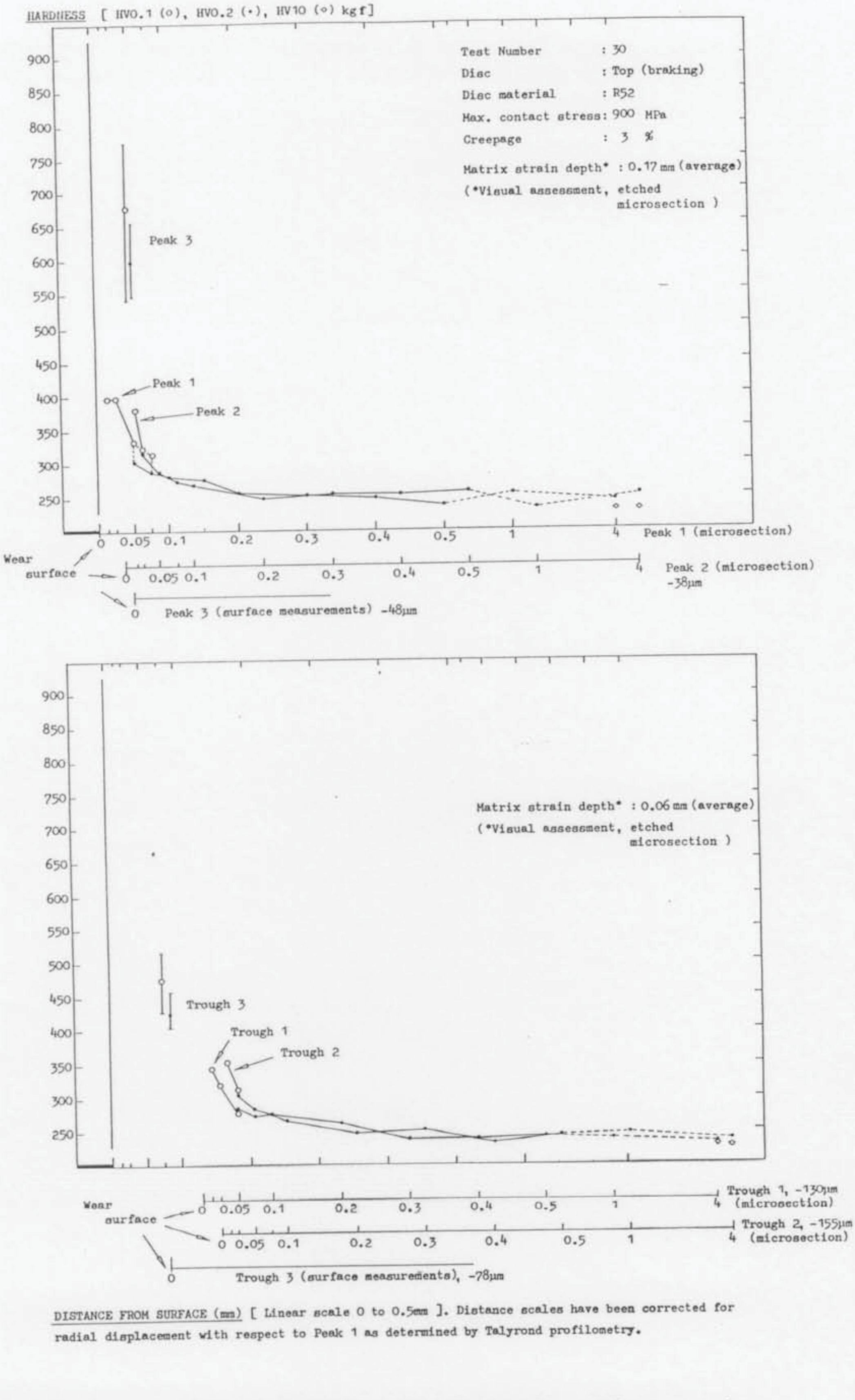

Figure 9.16 Microhardness profiles of the R52 top disc facet peak and facet trough wear surface circumferential sections shown in Figures 9.14 and 9.15, respectively. The offset in the "depth below surface" axes reflects radial diplacement of facet undulations, with all equivalent points being equidistant from the disc centre.

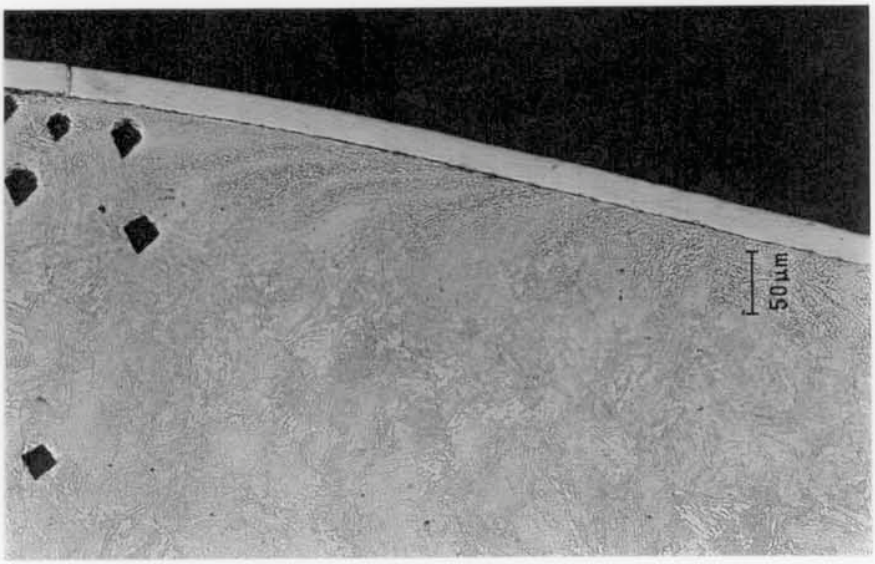

a
(x170 mag.)

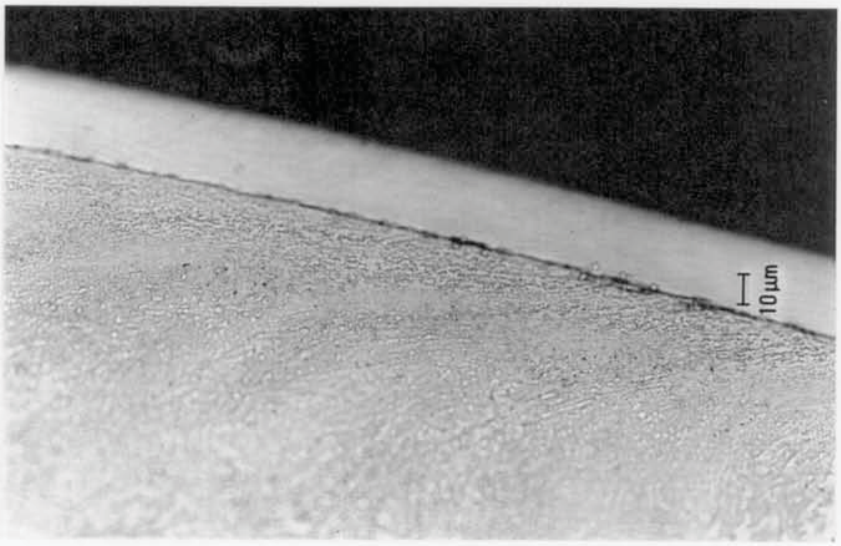

b
(x425 mag.)

Figure 9.17 Wear surface circumferential section through a B20 top driven disc, LEROS tested at 900 MPa p_o and 3% γ (Test 37). *Section through a facet peak.*

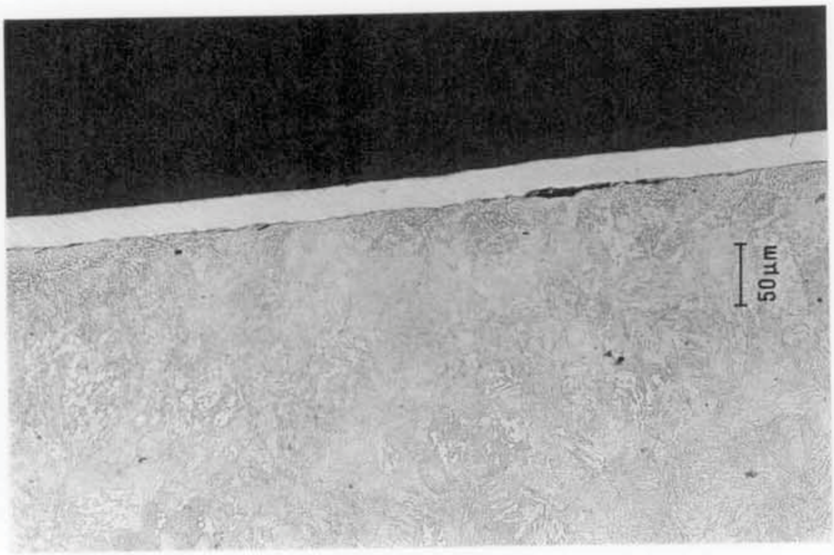

a
(x170 mag.)

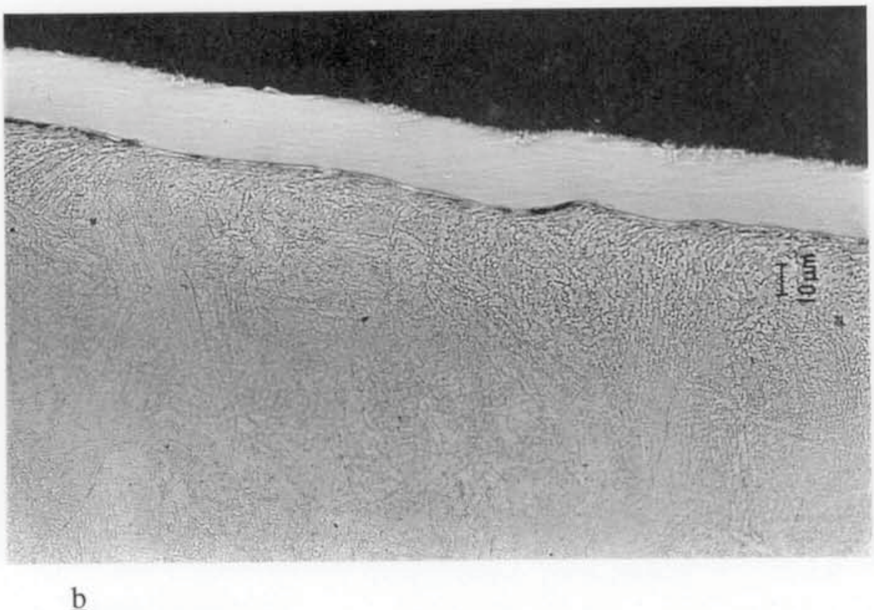

b
(x425 mag.)

Figure 9.18 Wear surface circumferential section through a B20 top driven disc, LEROS tested at 900 MPa p_o and 3% γ (Test 37). *Section through a facet trough*. Less ratchetting than seen on the facet peak.

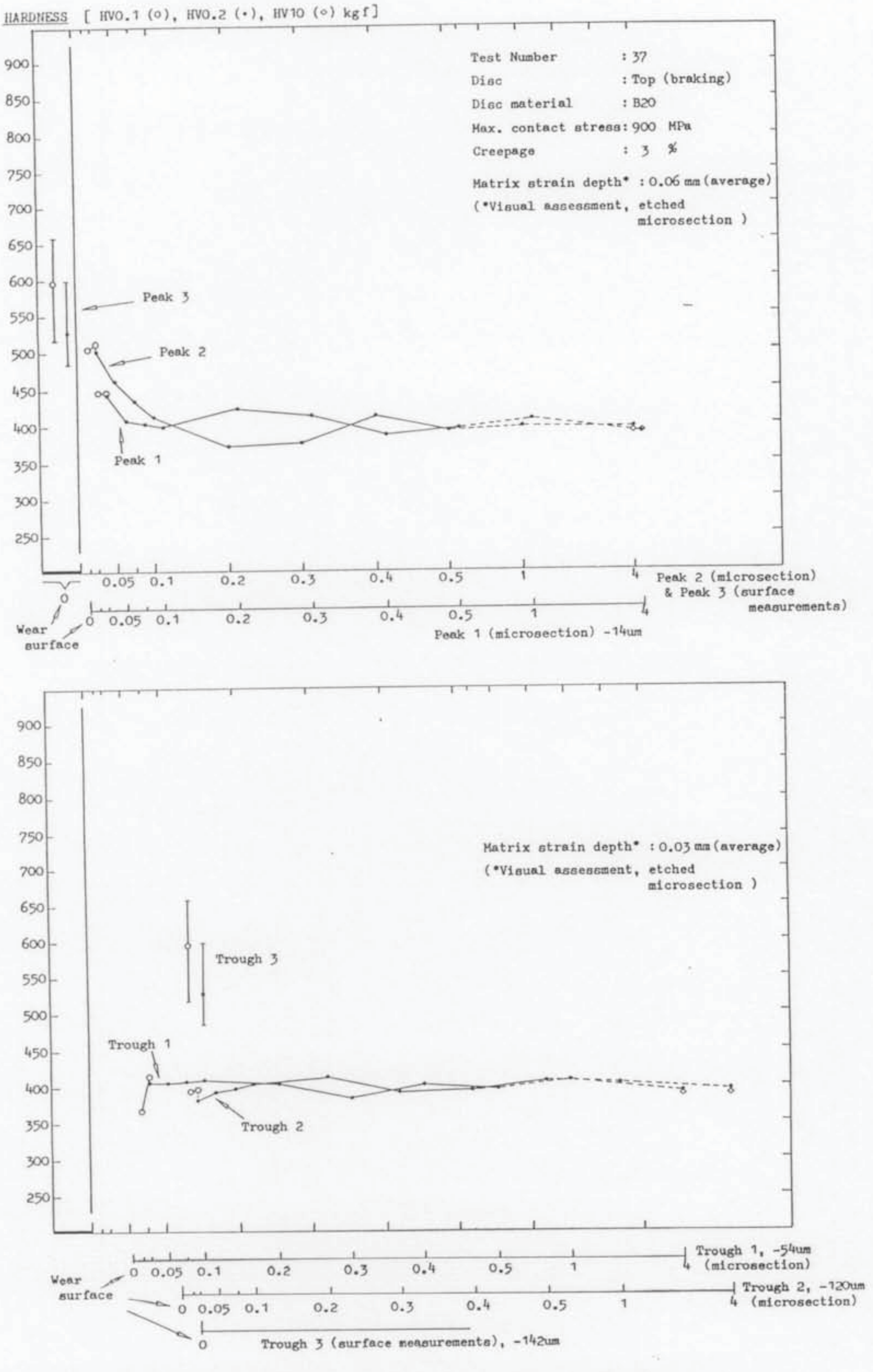

Figure 9.19 Microhardness profiles of the B20 top disc facet peak and facet trough wear surface circumferential sections shown in Figures 9.17 and 9.18, respectively. The offset in "depth below surface" axes reflects radial diplacement of facet undulations, with all equivalent points being equidistant from the disc centre.

a
(x42.5 mag.)

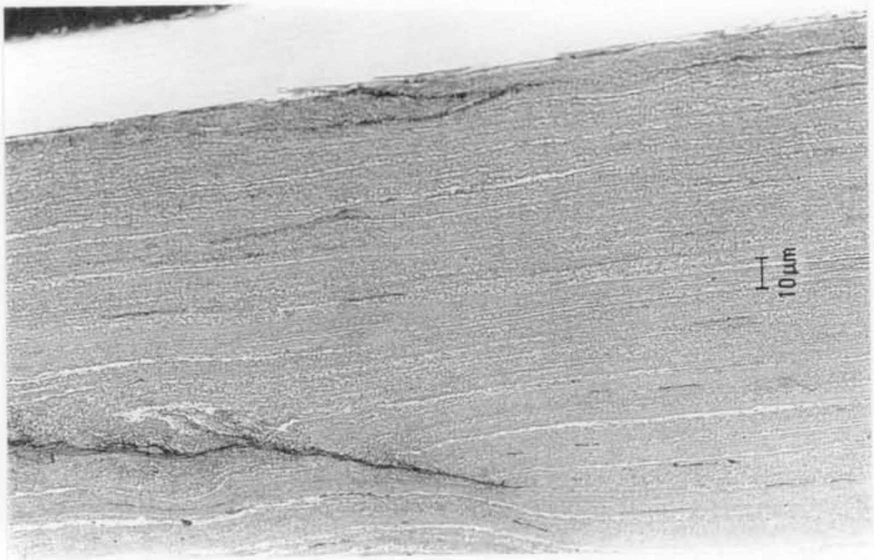

b
(x425 mag.)

Figure 9.20 Wear surface circumferential section through a R52 top driven disc, LEROS tested at 1800 MPa p_o and 1.5% γ (Test 46). This disc is shown in Figure 8.8.
(a) Overview showing the deep and thorough degree of ratchetting and pronounced surface flaking.
(b) Detail showing aligned matrix by a flake root and alignment disruption from crack face friction.
(c, d) Shown overleaf....

c
(x425 mag.)

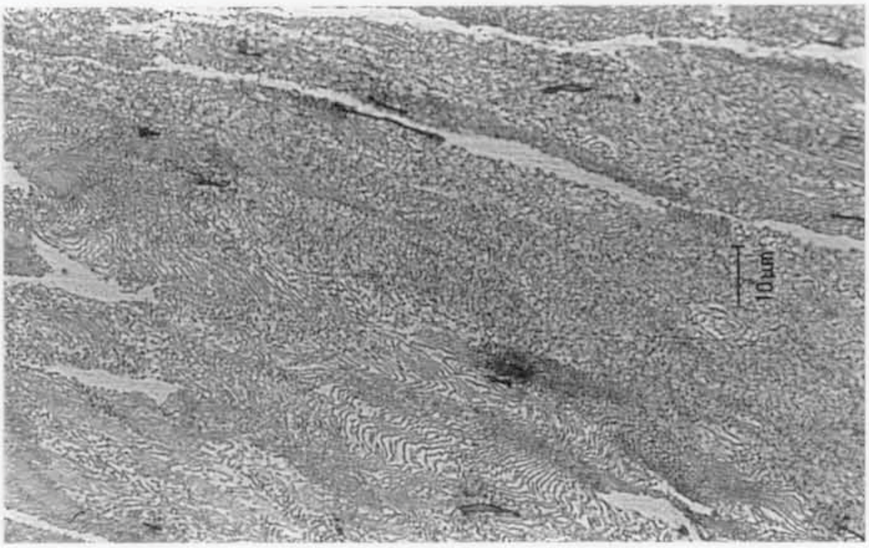

d
(x850 mag.)

Figure 9.20 continued...

(c) Ratchetting alignment of pearlite lamellae 0.33mm sub-surface and
(d) 0.56mm sub-surface.

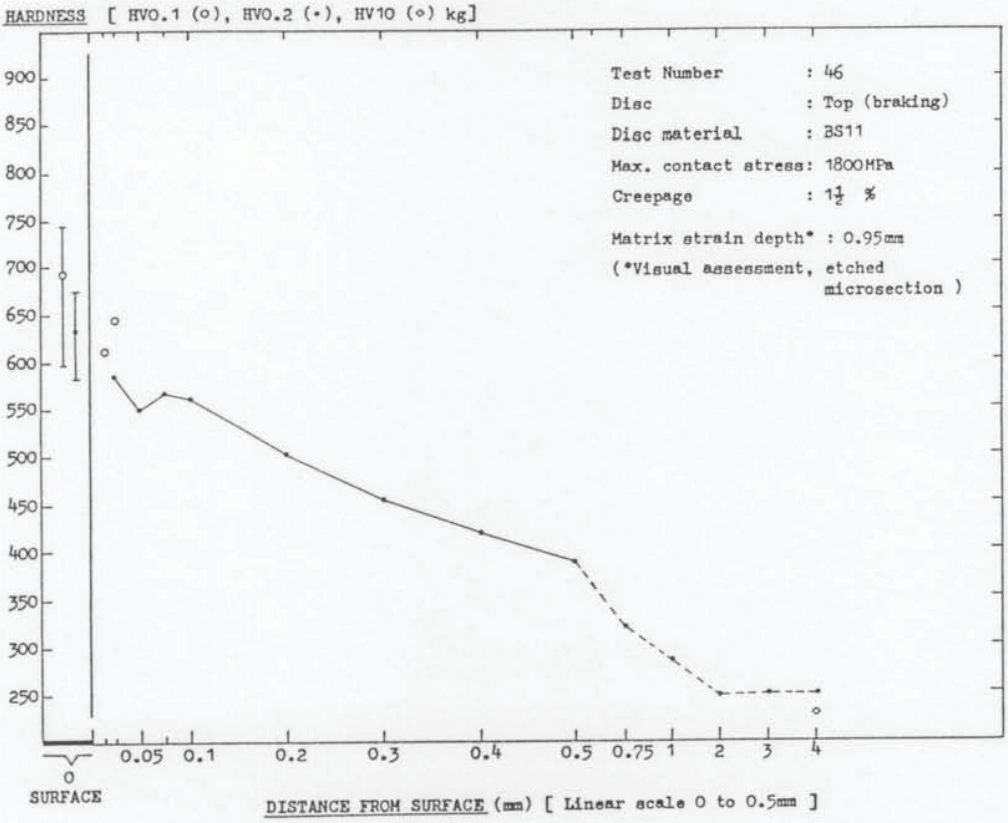

Figure 9.21 Microhardness profile of the R52 top disc wear surface circumferential section shown in Figures 9.20.

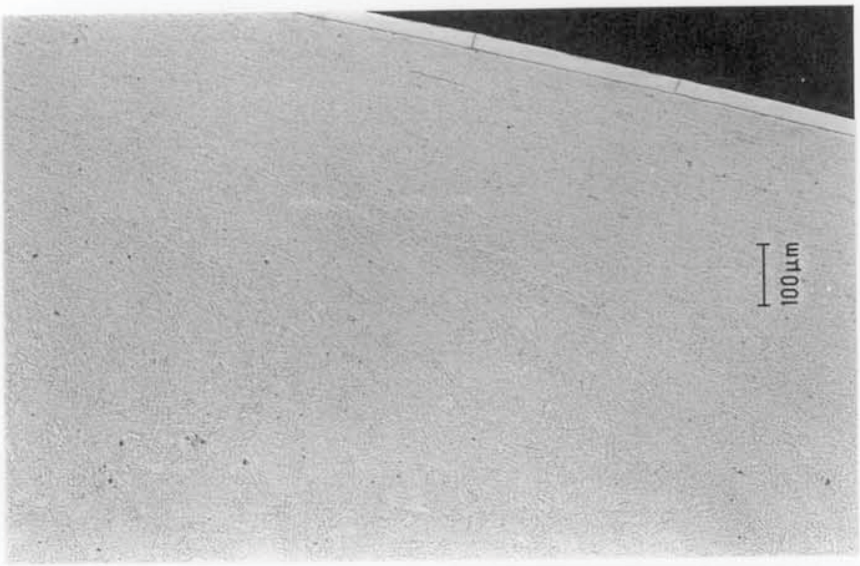

a
(x85 mag.)

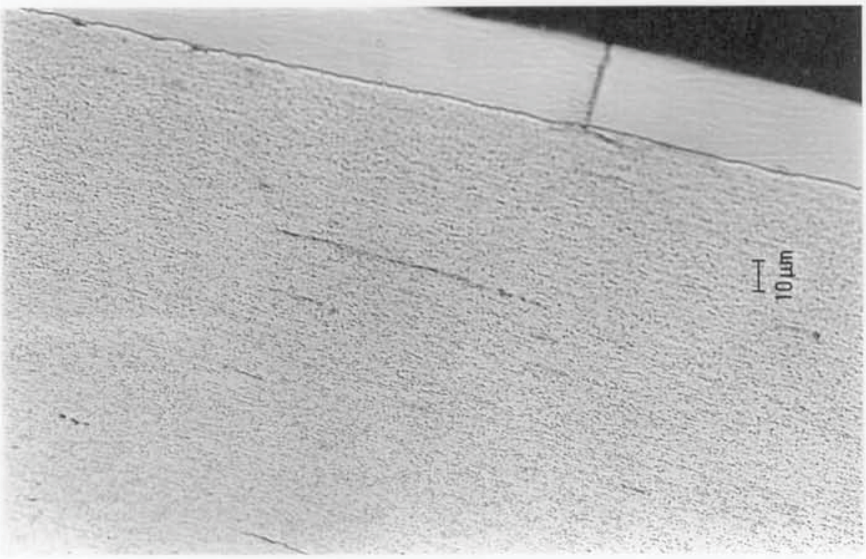

b
(x425 mag.)

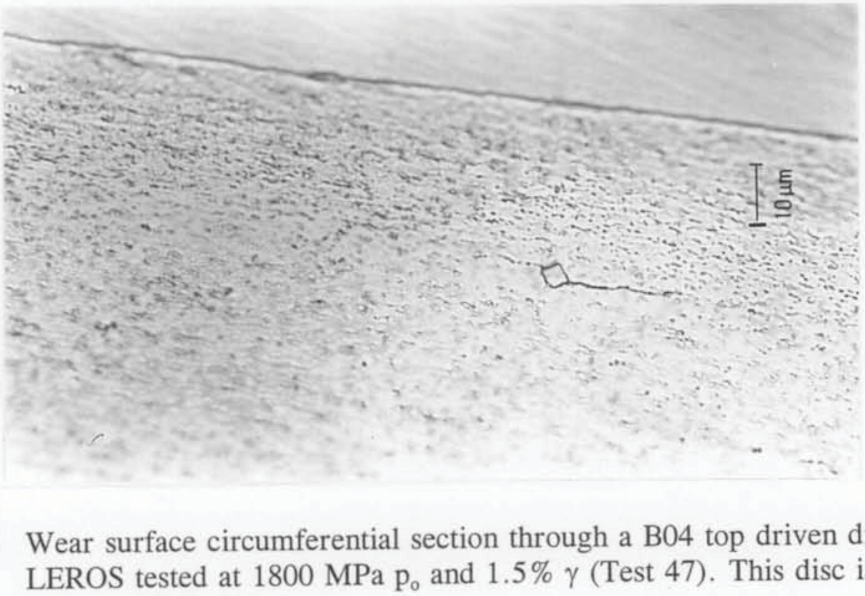

c
(x850 mag.)

Figure 9.22 Wear surface circumferential section through a B04 top driven disc, LEROS tested at 1800 MPa p_o and 1.5% γ (Test 47). This disc is shown in Figure 8.36.
(a) Overview showing ratchetting beneath smooth surface.
(b) Near-surface detail showing small pancaked MnS inclusions and a tiny surface flake.
(c) Near-surface detail showing crack intiation on a brittle Ti-based inclusion.

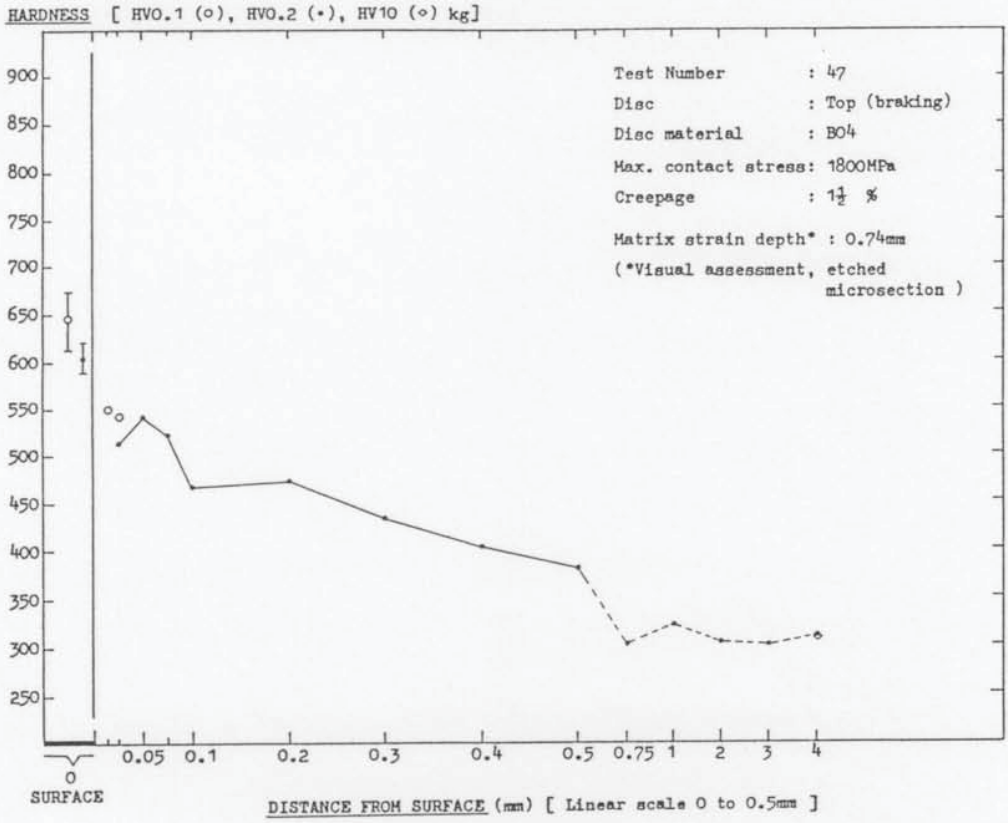

Figure 9.23 Microhardness profile of the B04 top disc wear surface circumferential section shown in Figures 9.22.

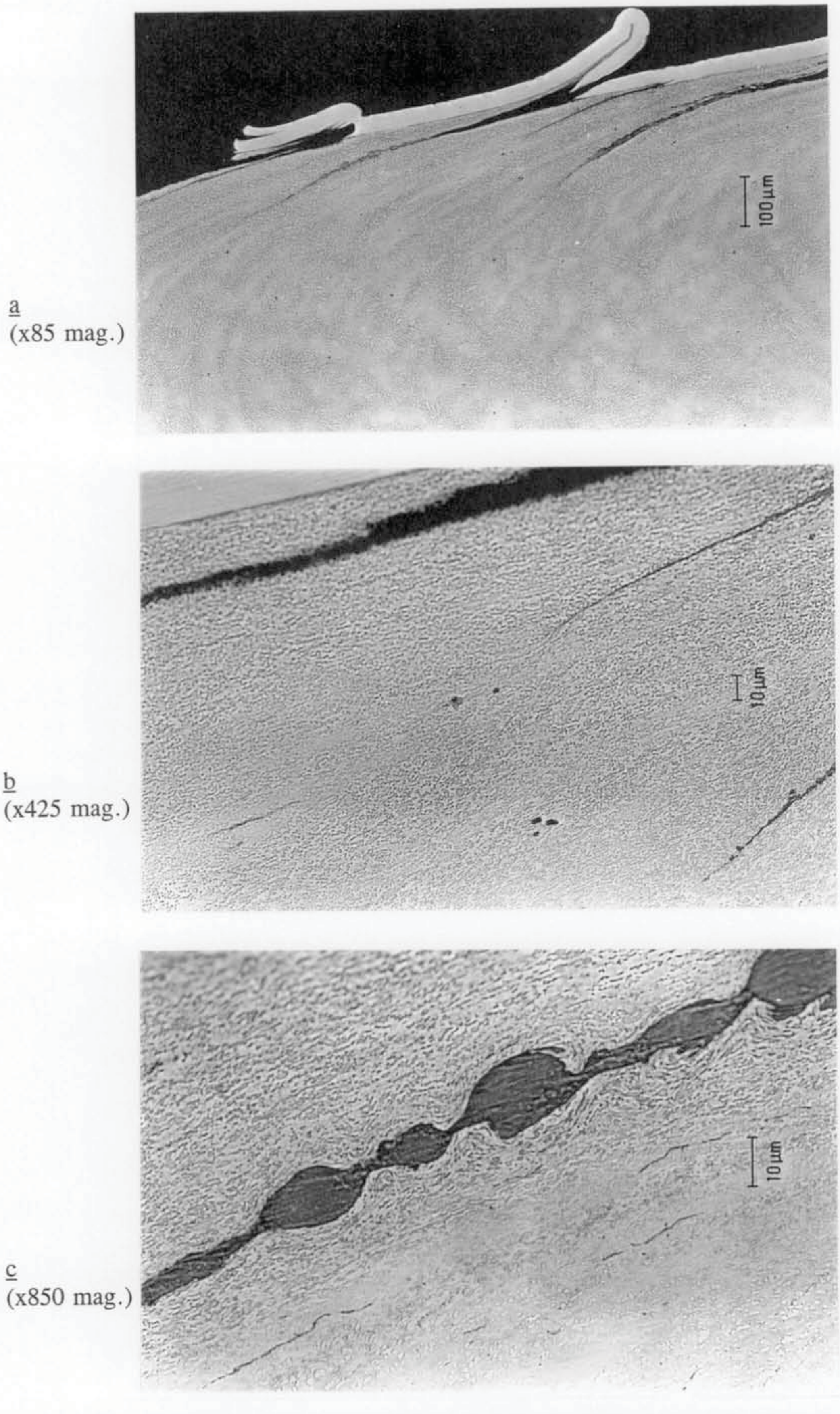

Figure 9.24 Wear surface circumferential section through a B20 top driven disc, LEROS tested at 1800 MPa p_o and 1.5% γ (Test 48). This disc is shown in Figure 8.37a.
(a) Overview showing ratchetting and strongly adhering surface flakes.
(b) Detail of ratchetted structure.
(c) Aligned matrix disruption due to crack face friction.

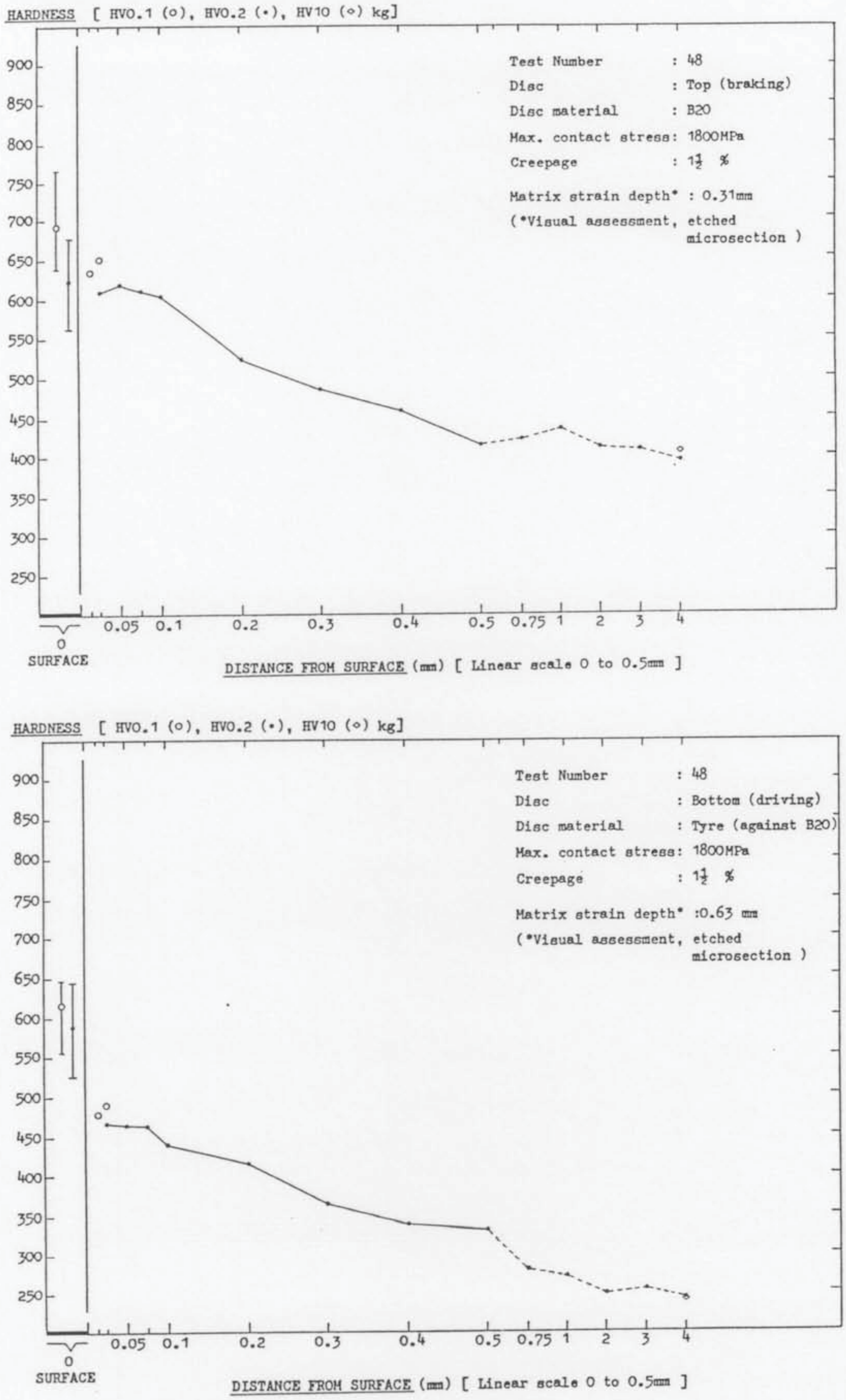

Figure 9.25 Microhardness profile of the B20 top disc wear surface circumferential section shown in Figures 9.24.

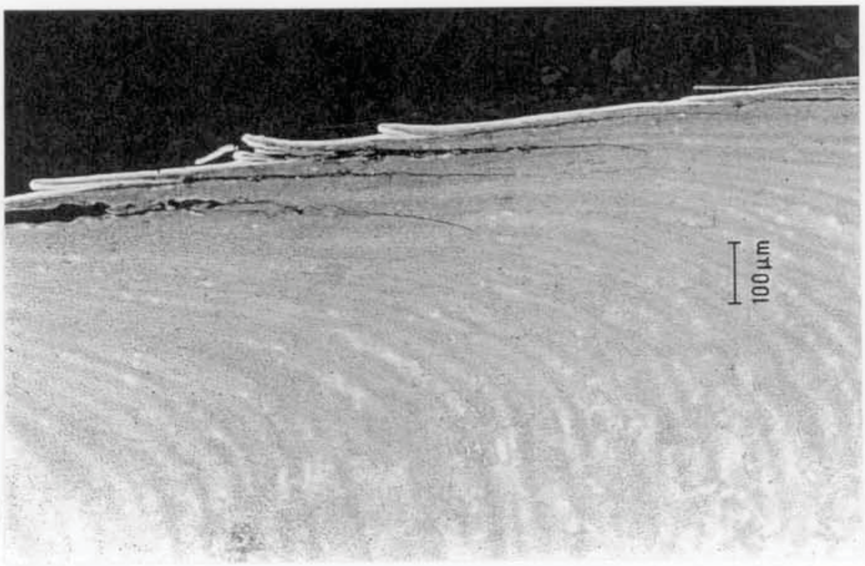

a
(x85 mag.)

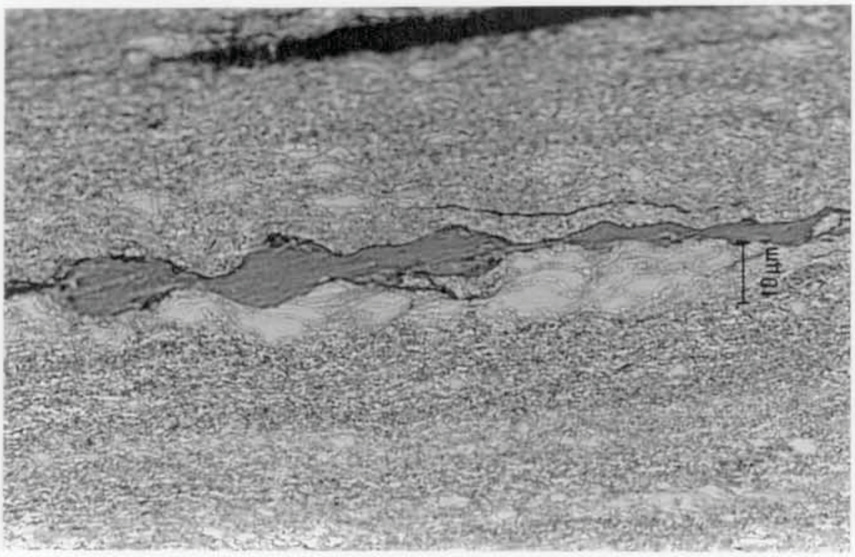

b
(x850 mag.)

Figure 9.26 Wear surface circumferential section through a B52 top driven disc, LEROS tested at 1800 MPa p_o and 1.5% γ (Test 49). This disc is shown in Figure 8.37b.
(a) Overview showing ratchetting and dense surface flaking.
(b) Detail of flake crack showing disruption of matrix alignment from crack face friction and rigid lower bainite / martensite zones. These have begun to deform near the surface.
(c, d) Shown overleaf....

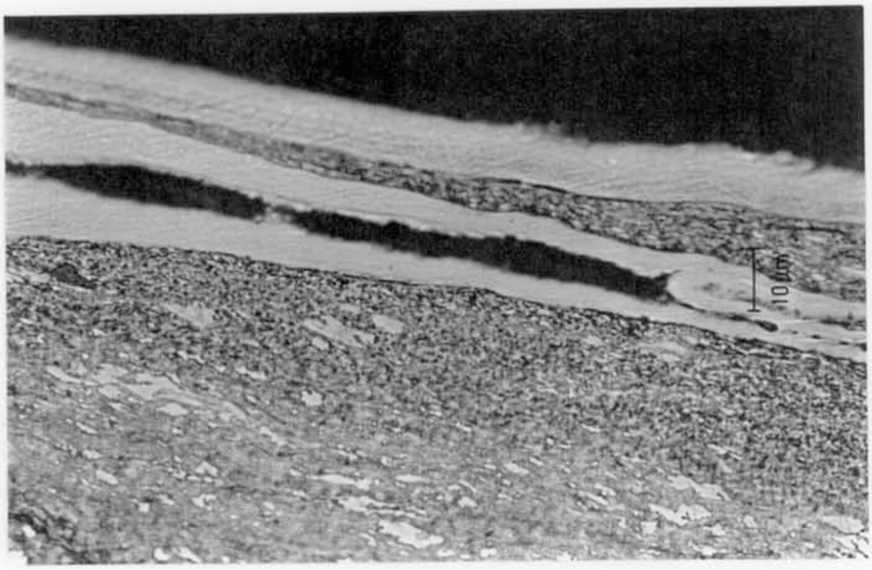

c
(x850 mag.)

d
(x850 mag.)

Figure 9.26 continued.....

(c) Deformation and strain alignment of all parts of the structure at the surface.
(d) Ratchetted structure 0.12mm sub-surface and crack initiation on a brittle, fractured Ti-based inclusion.

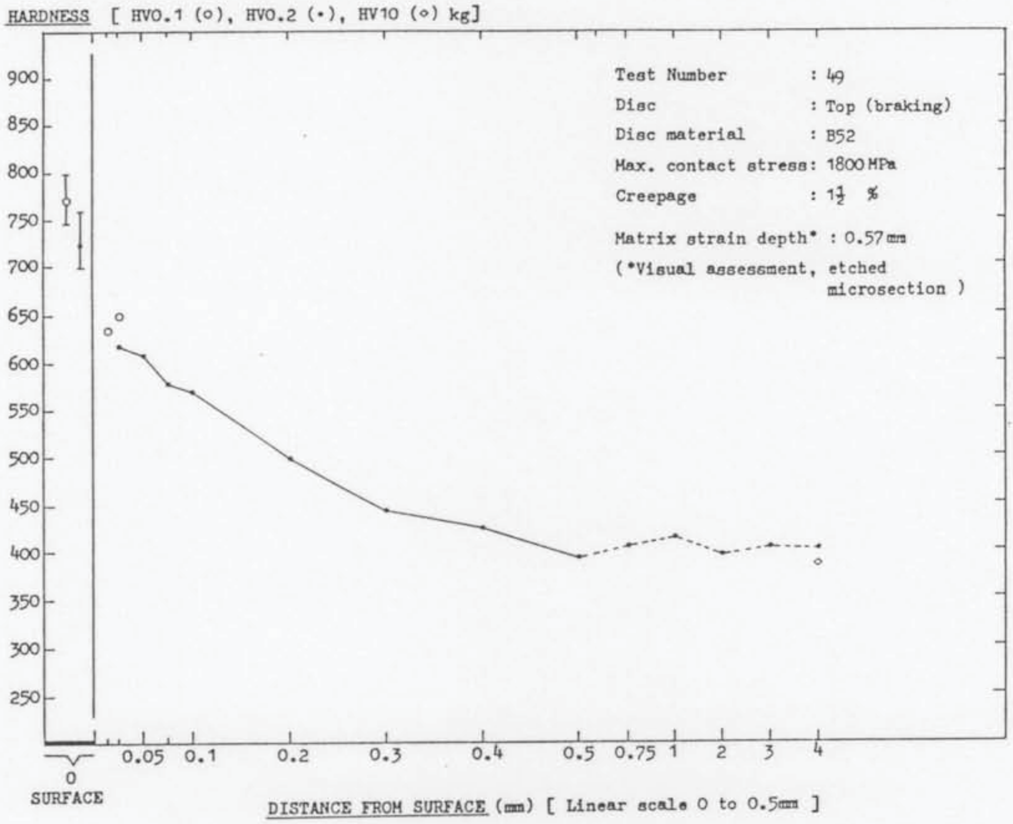

Figure 9.27 Microhardness profile of the B52 top disc wear surface circumferential section shown in Figures 9.26.

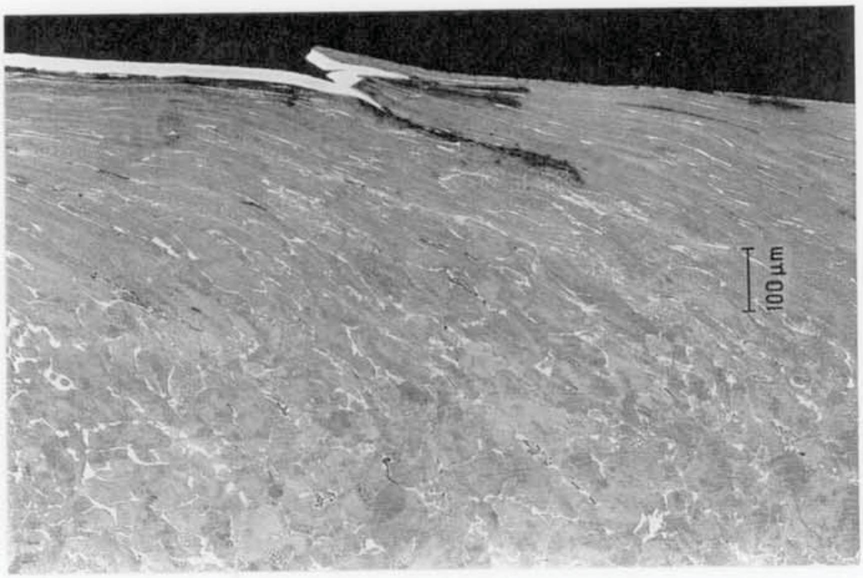

a
(x85 mag.)

b
(x170 mag.)

Figure 9.28 Wear surface circumferential section through a W64 bottom driving disc, LEROS tested against B20 at 1800 MPa p_o and 1.5% γ (Test 48). Surface shown in Figure 8.39.
(a) Duplex flaking, thick truncated flakes.
(b) Surface fatigue fracture down to crack plane along pancaked MnS.
(c, d) Shown overleaf...

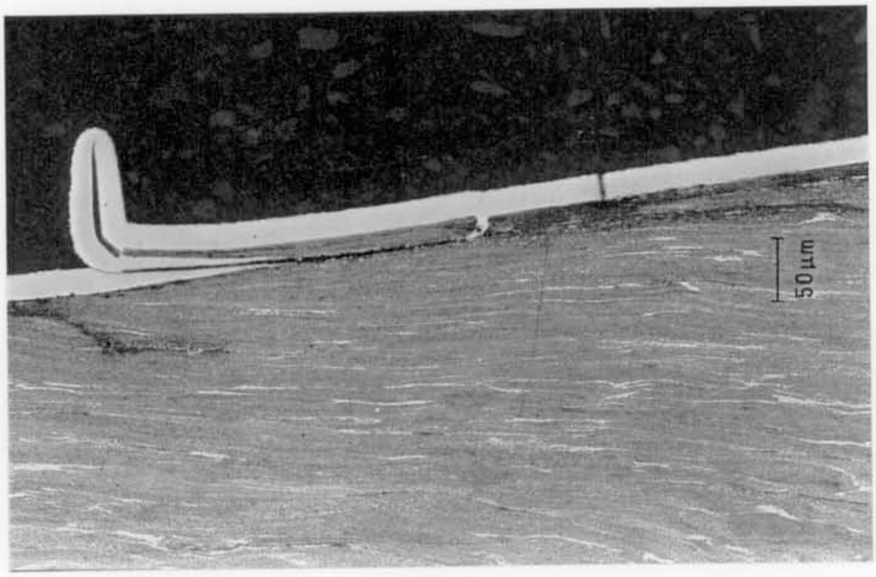

c
(x170 mag.)

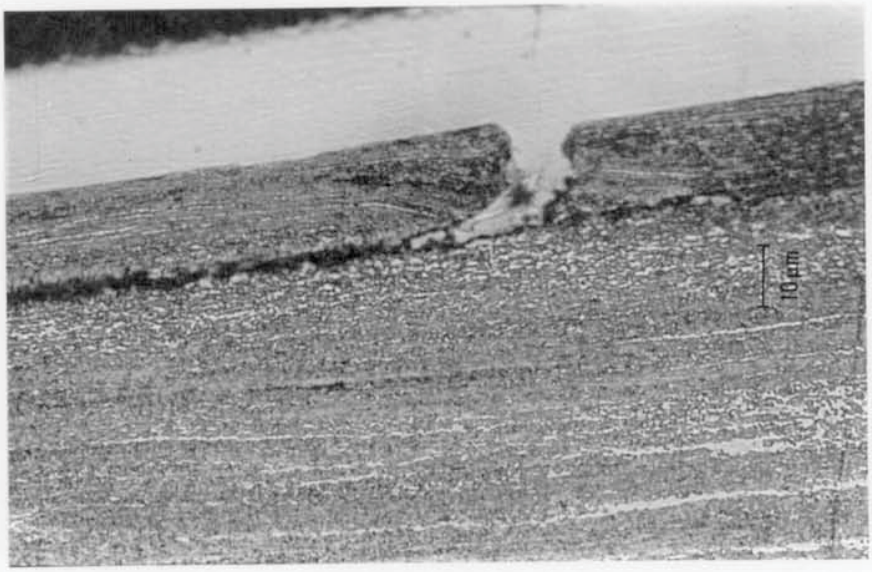

d
(x850 mag.)

Figure 9.28 continued…

(c and d) Block fracture of a flake and, to the left, another crack down to a crack plane initiated along pancaked MnS.

a
(x170 mag.)

b
(x425 mag.)

Figure 9.29 Wear surface circumferential section through a W64 bottom driving disc, LEROS tested against R52 at 1300 MPa p_o and 10% γ (Test 42). (a) Overview showing undulating surface and some debris adherence. (b) The ratchetted structure near the undulating surface.

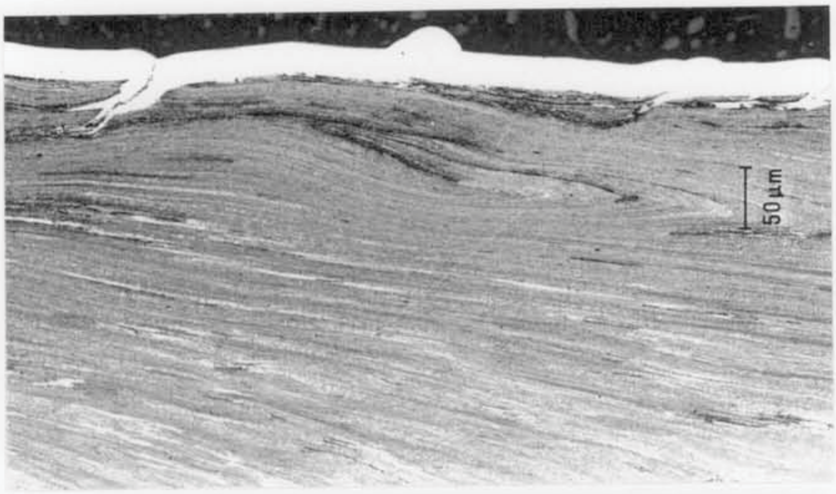

a
(x170 mag.)

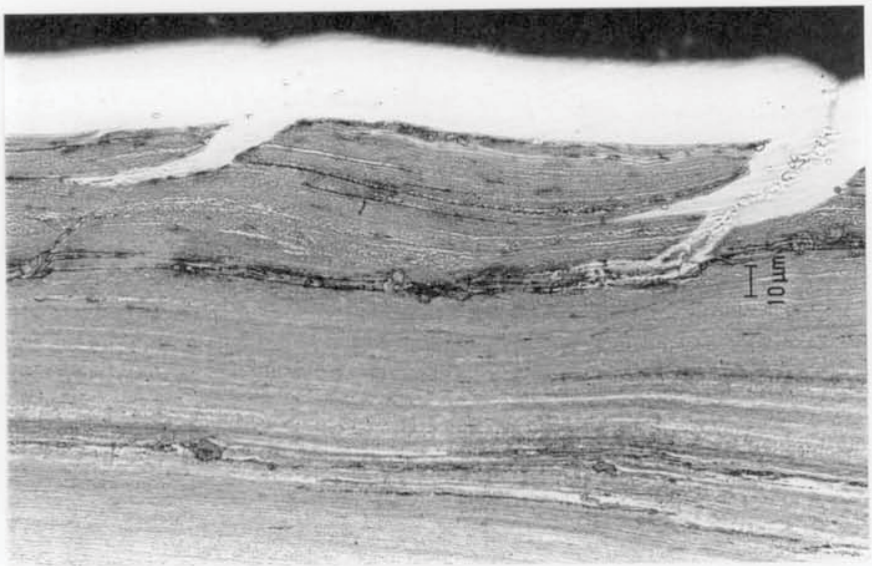

b
(x425 mag.)

c
(x425 mag.)

Figure 9.30 Wear surface circumferential section through a W64 bottom driving disc, LEROS tested against B20 at 1300 MPa p_o and 10% γ (Test 44). The disc surface is shown in Figure 8.56.
(a) Overview showing a far more ratchetted structure than seen in Figure 9.29 and, again, fatigue fracture down from the surface to crack planes based on pancaked MnS inclusions.
(b) Detail of fatigue fracture.
(c) Detail of material flow between the surface and a sub-surface crack plane.

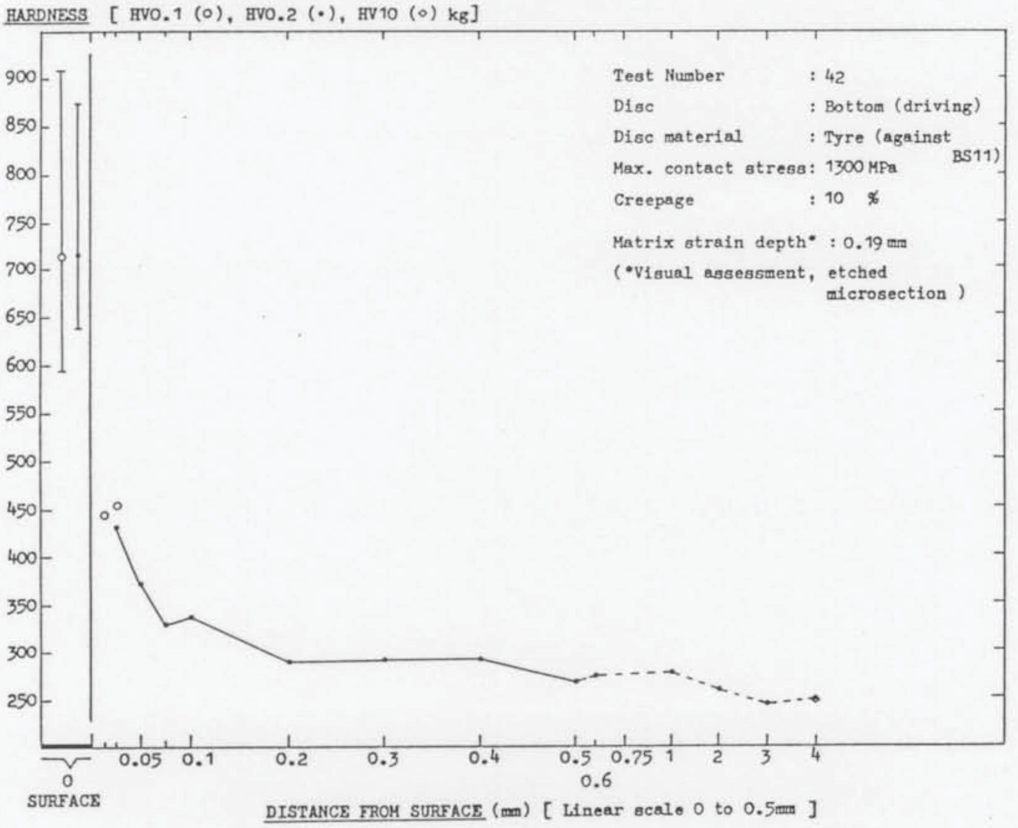

Figure 9.31 Microhardness profile of the W64 bottom disc wear surface circumferential section shown in Figure 9.29.

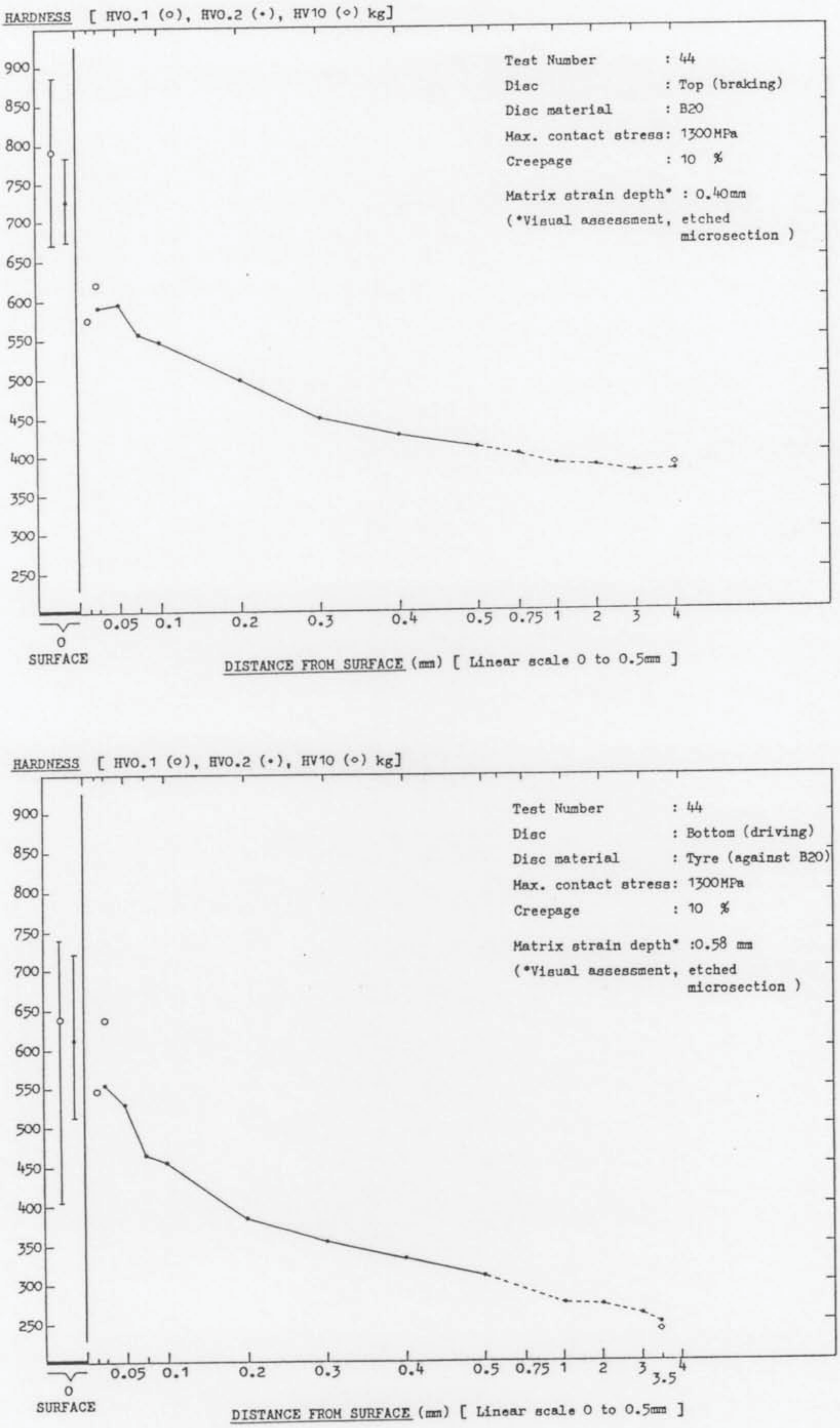

Figure 9.32 Microhardness profiles of the B20 top disc and W64 bottom disc wear surface circumferential sections shown in Figures 9.33 and 9.30, respectively (Test 44).

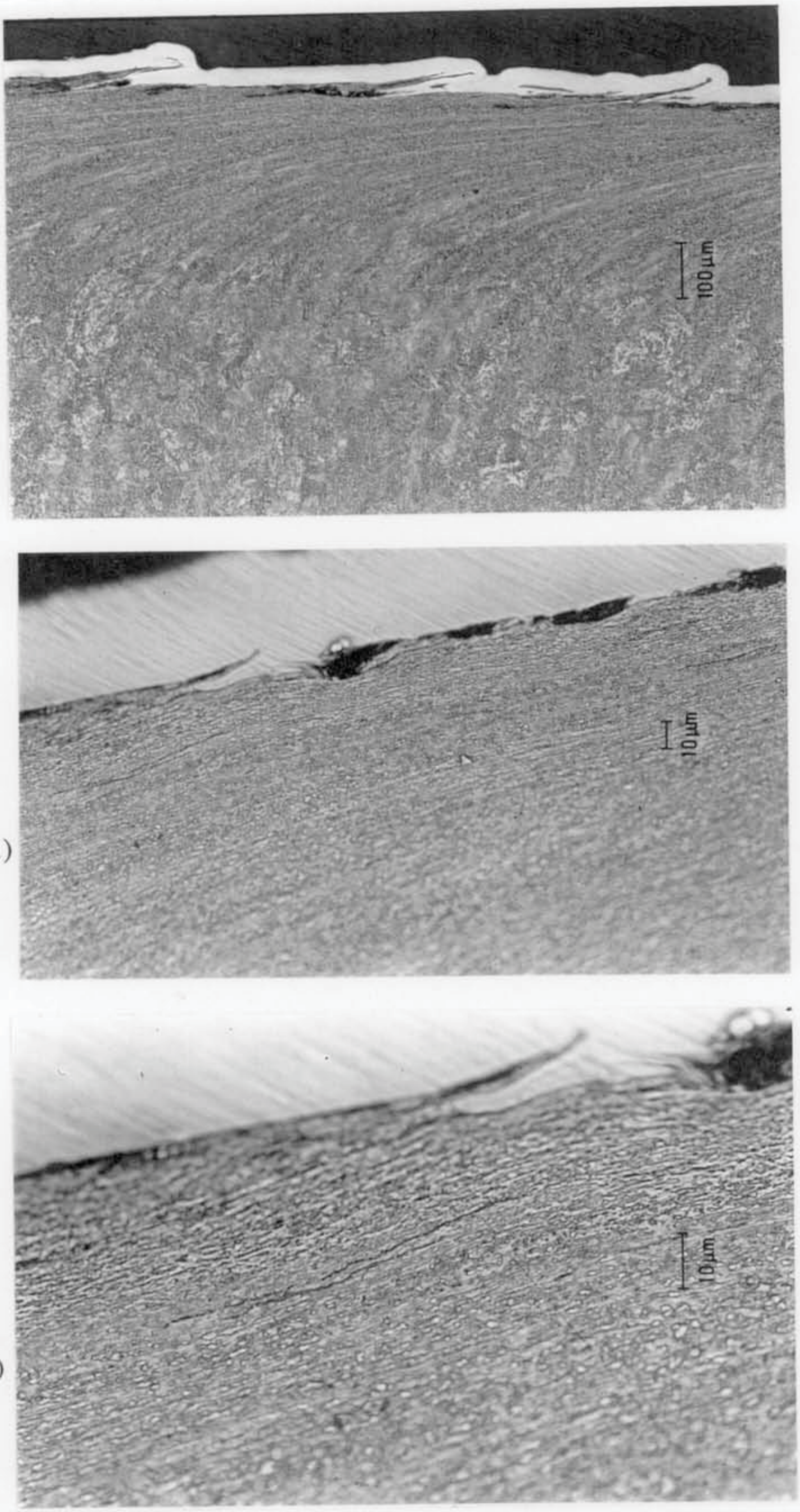

a
(x85 mag.)

b
(x425 mag.)

c
(x850 mag.)

Figure 9.33 Wear surface circumferential section through a B20 top driven disc, LEROS tested at 1300 MPa p_o and 10% γ (Test 44). The disc surface is shown in Figures 7.17c and 8.57.
(a) Overview of ratchetted structure and surface flaking.
(b) Detail of aligned MA phase near the surface.
(c) Detail of fine, pancaked MnS. Here, no planar cracks have been initiated.

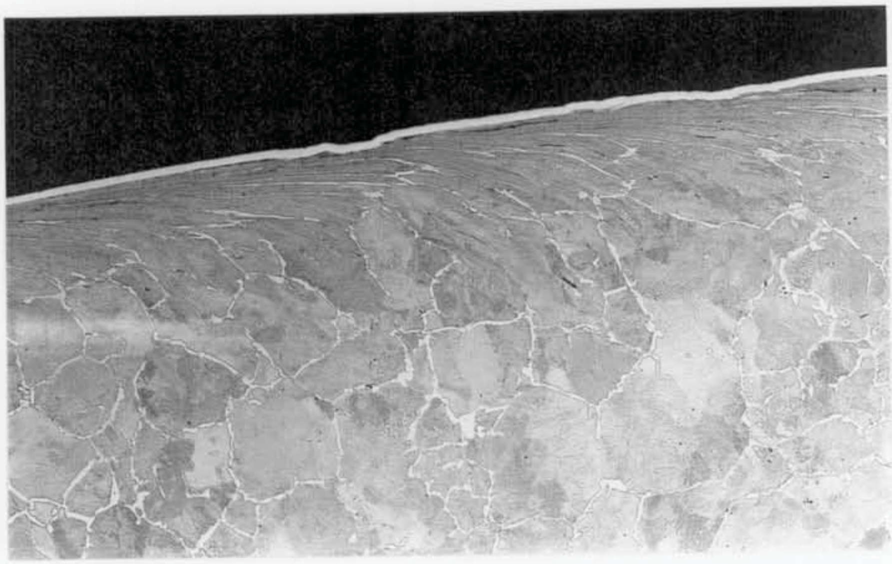

a
(x85 mag.)

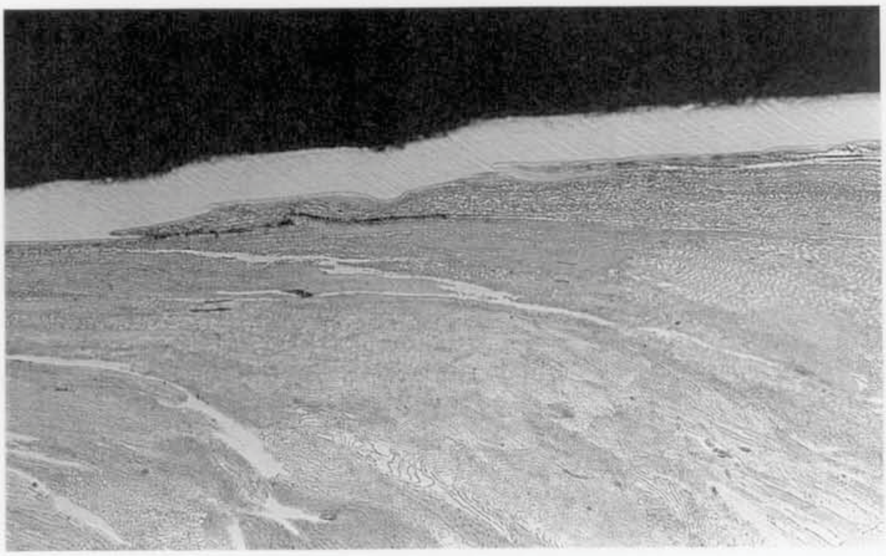

b
(x425 mag.)

Figure 9.34 Wear surface circumferential section through a R52 top driven disc, Amsler tested at 884 MPa p_o and 10% γ (Test 25). The disc surface is shown in Figures 8.47b and 8.51a.
(a) Overview, ratchetting beneath undulating surface.
(b) Detail of short surface flakes.

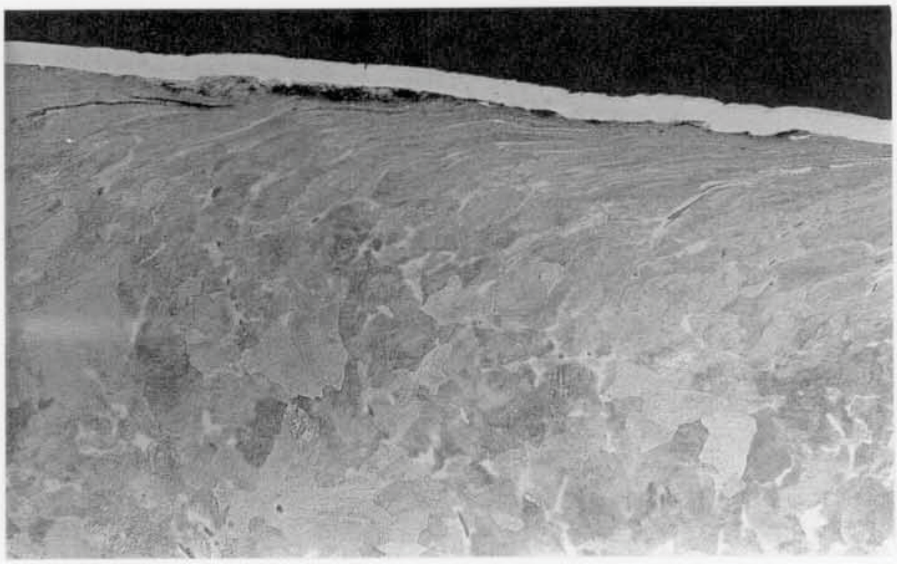

a
(x85 mag.)

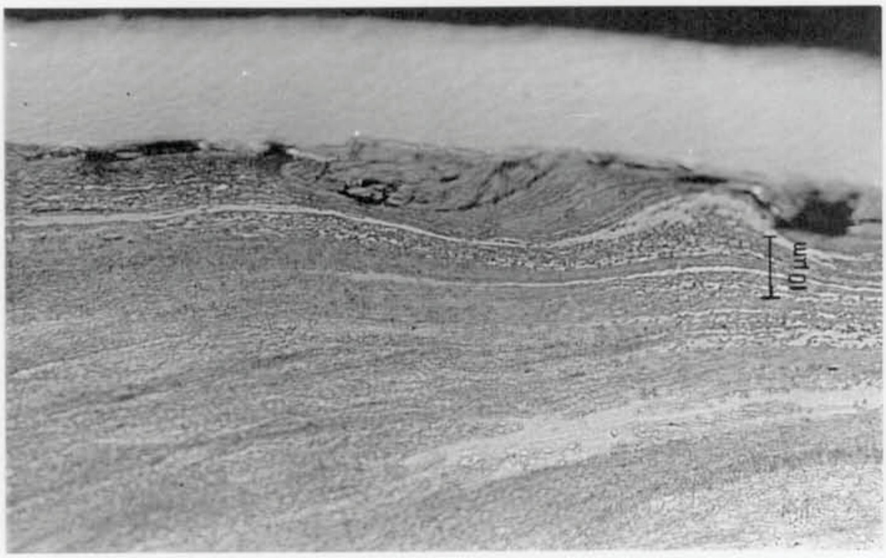

b
(x850 mag.)

Figure 9.35 Wear surface circumferential section through a W64 bottom driving disc, Amsler tested against R52 at 884 MPa p_o and 10% γ (Test 25). The disc surface is shown in Figure 8.47b.
(a) Overview, ratchetting beneath undulating surface.
(b) Surface detail, adhered debris.

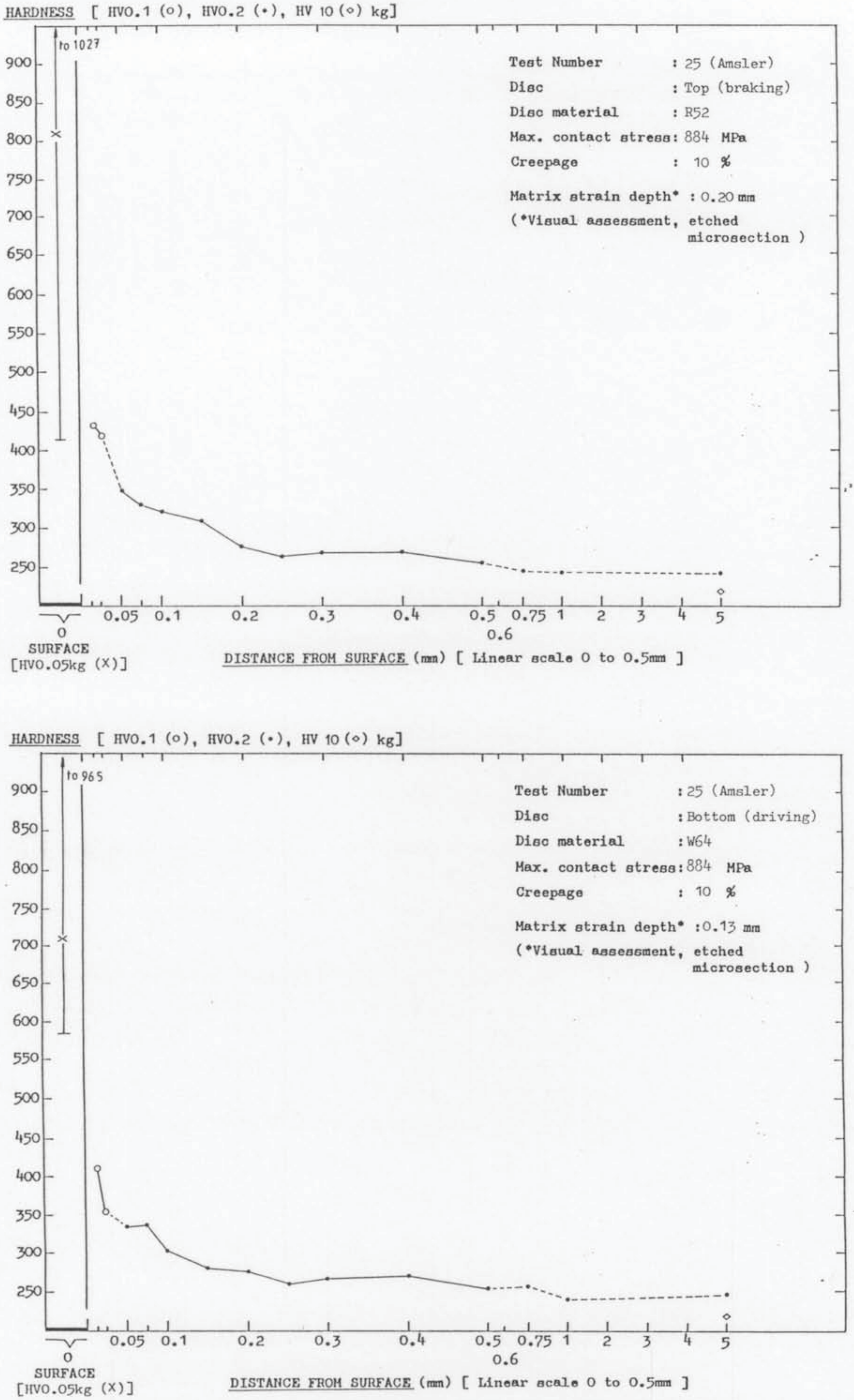

Figure 9.36 Microhardness profiles of the R52 top disc and W64 bottom disc wear surface circumferential sections shown in Figures 9.34 and 9.35, respectively (Test 25). Marked hardening just at the surface.

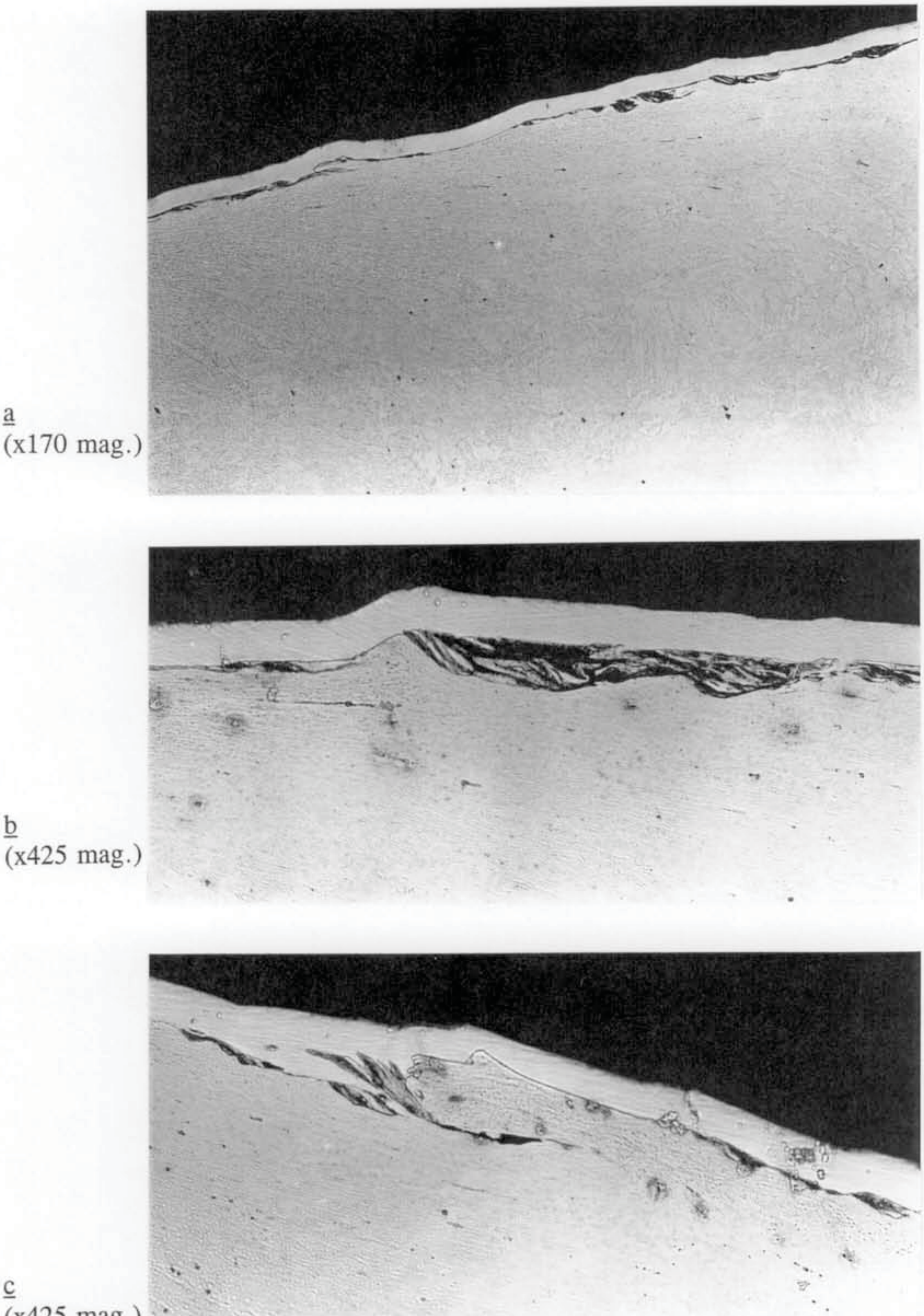

Figure 9.37 Wear surface circumferential section through a B04 top driven disc, Amsler tested at 884 MPa p_o and 10% γ (Test 23). The disc surface is shown in Figure 8.51b.
(a) Overview of ratchetted structure and undulating surface with adhered debris.
(b) Detail of adhered debris.
(c) Detail of truncated flake which appears to have "machined" the counter surface.

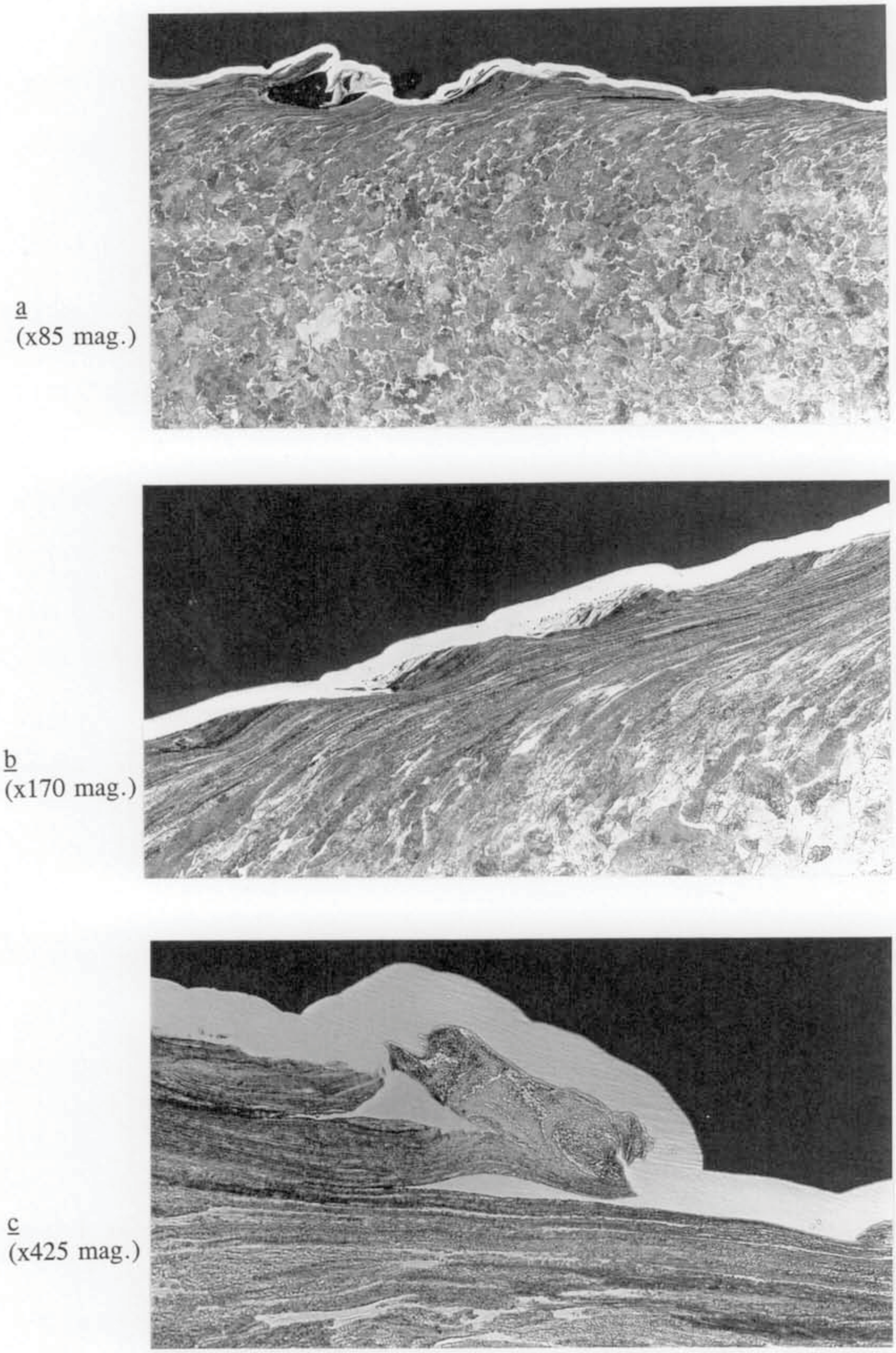

Figure 9.38 Wear surface circumferential section through a W64 bottom driving disc, Amsler tested against B04 at 884 MPa p_o and 10% γ (Test 23).
(a) Overview showing ratchetting and severely undulating surface.
(b) Detail showing adhered debris between surface undulations.
(c) Detail showing material "scooped" and ploughed from the surface.

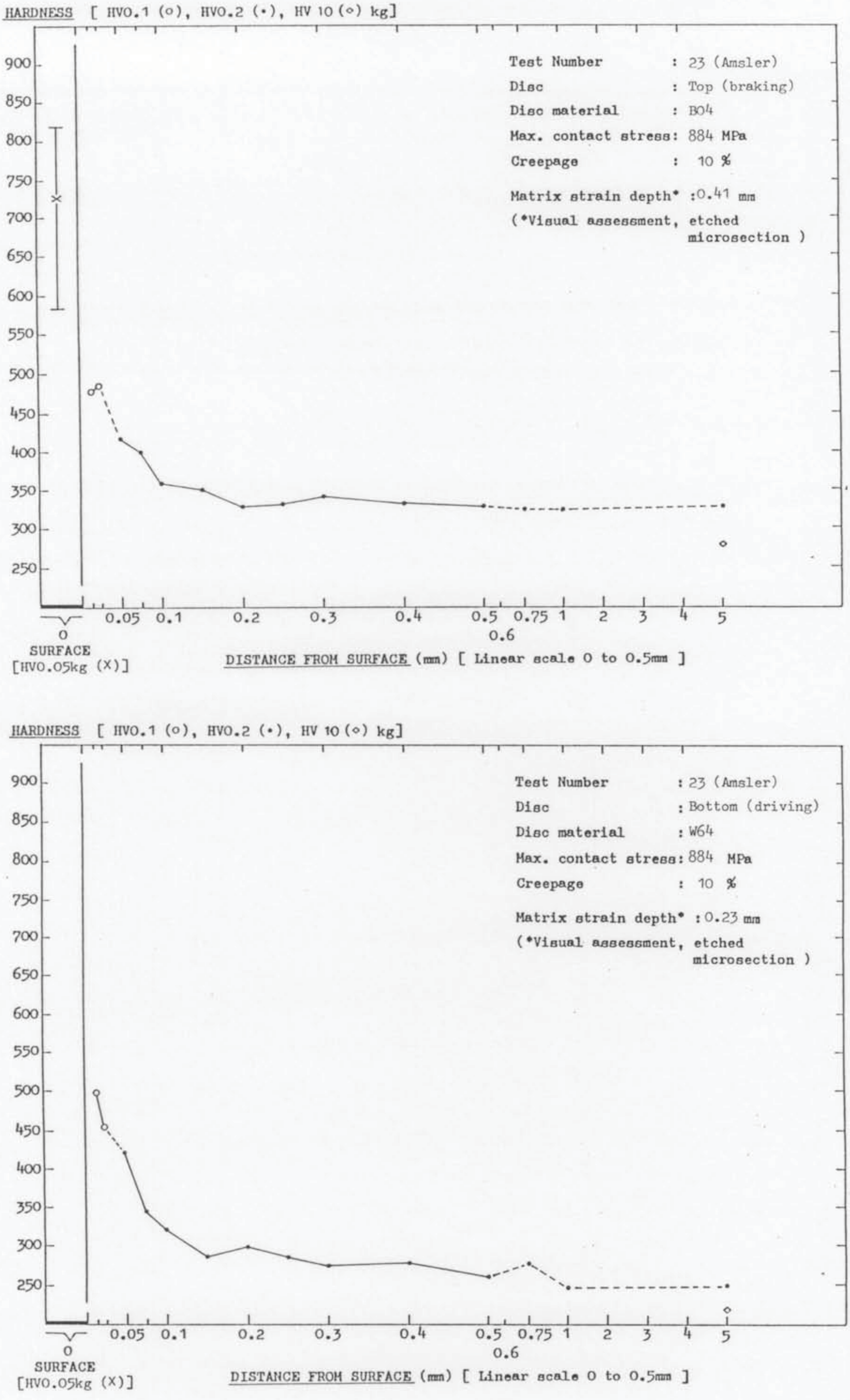

Figure 9.39 Microhardness profiles of the B04 top disc and W64 bottom disc wear surface circumferential sections shown in Figures 9.37 and 9.38, respectively (Test 23).

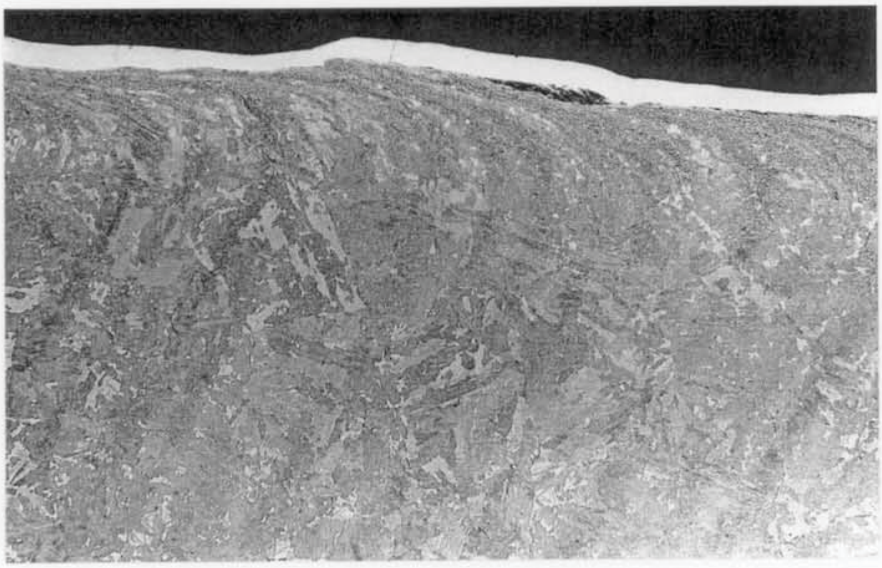

a
(x170 mag.)

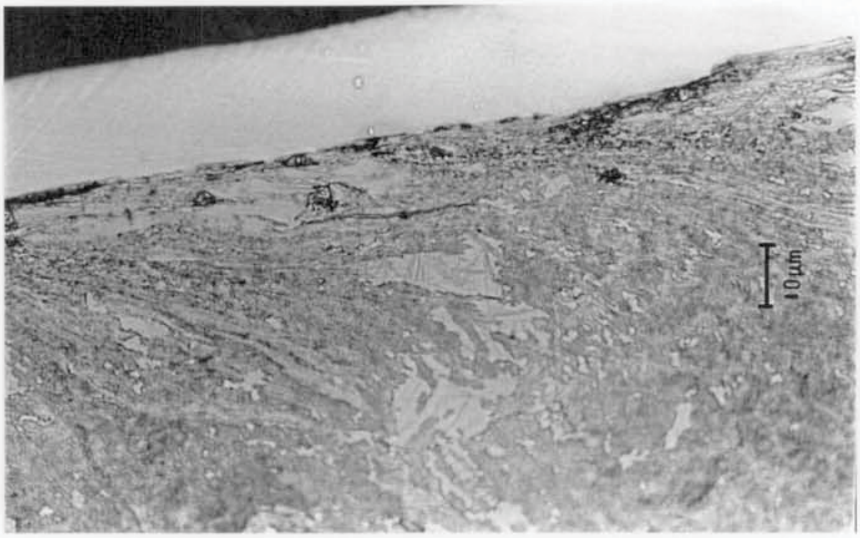

b
(x850 mag.)

Figure 9.40 Wear surface circumferential section through a B52 top driven disc, Amsler tested at 884 MPa p_o and 10% γ (Test 22). The disc surface is shown in Figure 8.51c.
(a) Overview of ratchetting, undulating surface and adhered debris.
(b) Detail of differential degree of matrix strain near the surface between the upper bainite areas (dark) and the lower bainite / martensite areas (light).

(x85 mag.)

Figure 9.41 Wear surface circumferential section through a W64 bottom driving disc, Amsler tested against B52 at 884 MPa p_o and 10% γ (Test 22). Overview of ratchetting and generation of thick flakes.

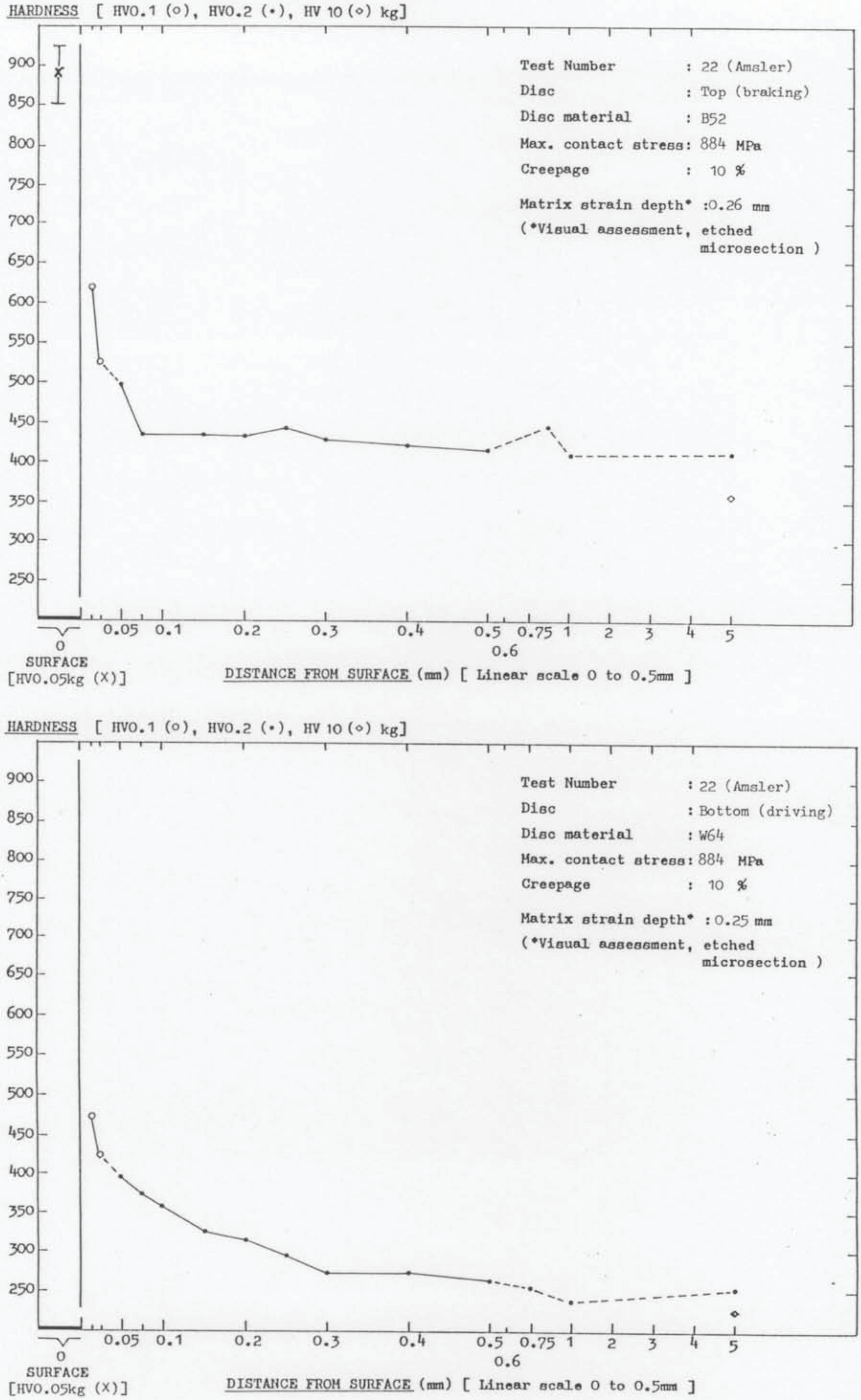

Figure 9.42 Microhardness profiles of the B52 top disc and W64 bottom disc wear surface circumferential sections shown in Figures 9.40 and 9.41, respectively (Test 22).

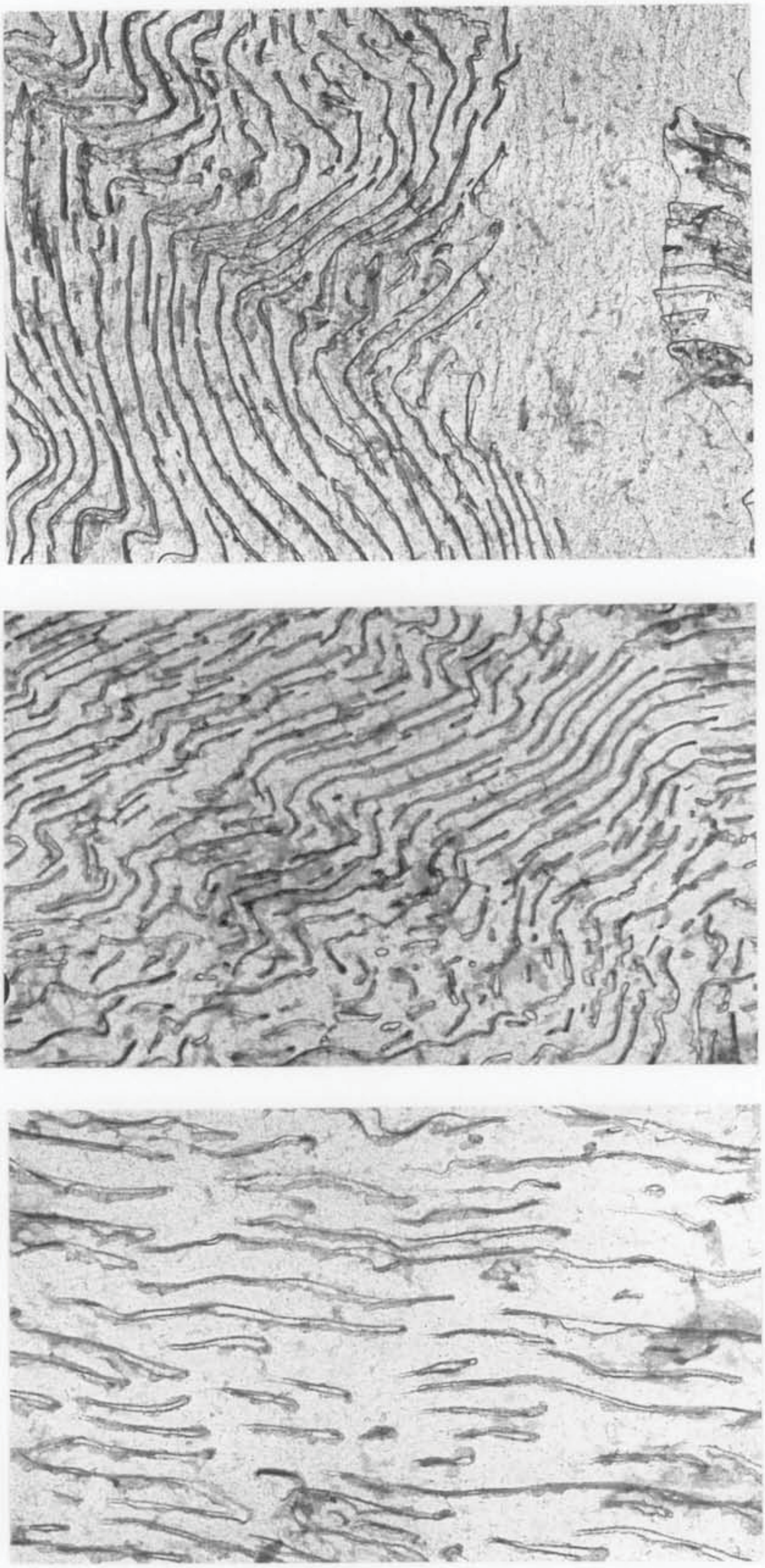

a
(x11760 mag.)

b
(x13000 mag.)

c
(x28600 mag.)

Figure 9.43 TEM micrographs of carbon replicas taken from the R52 top disc microsection shown in Figure 9.6 (Amsler test at 900 MPa p_o, 3% γ). (a) Cementite lamellae beginning to deform at around 0.5mm sub-surface. (b) Lamellae deformation around 0.25mm sub-surface. (c) Alignment of shorter lengths of lamellae within 0.02mm of the surface.

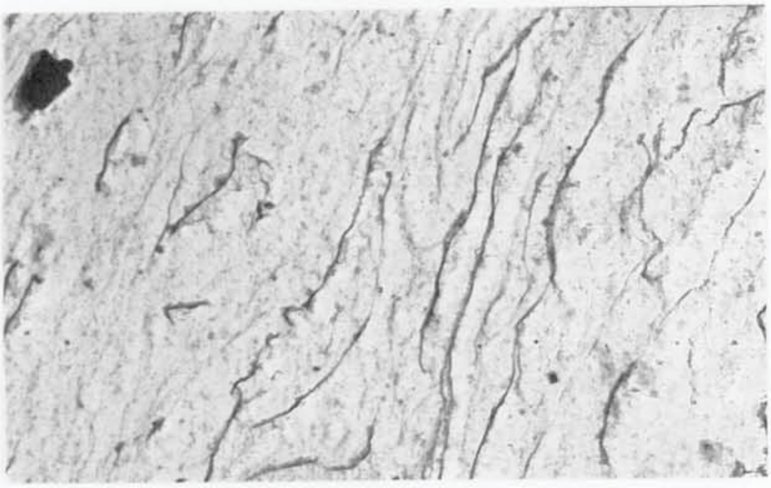

a
(x20800 mag.)

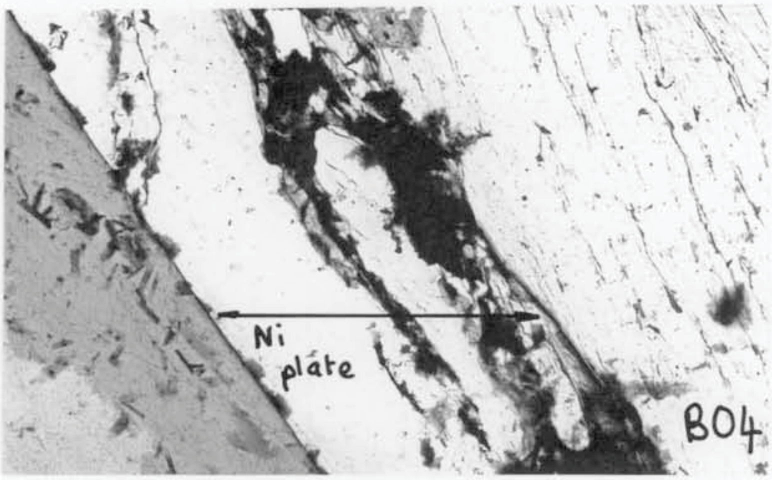

b
(x8580 mag.)

Figure 9.44 TEM micrographs of carbon replicas taken from the B04 top disc microsection shown in Figure 9.8 (Amsler test at 900 MPa p_o, 3% γ).
(a) Strain alignment and deformation of MA phase near the surface.
(b) The wear surface.

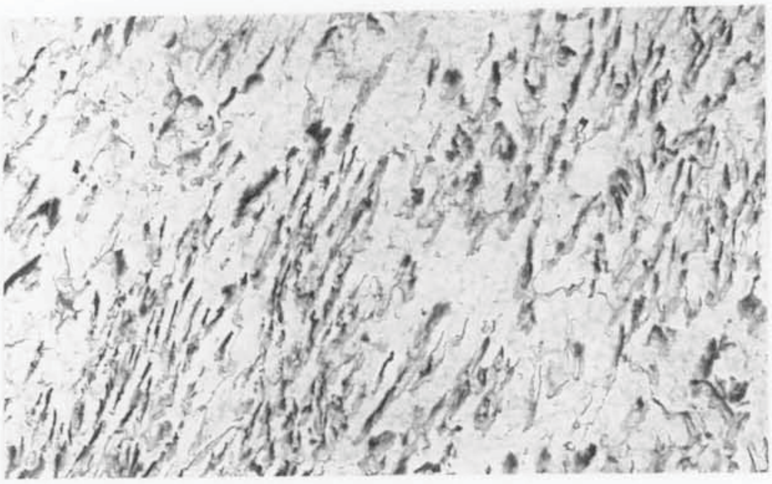

(x13000 mag.)

Figure 9.45 TEM micrographs of carbon replicas taken from the B52 top disc microsection shown in Figure 9.11 (Amsler test at 900 MPa p_o, 3% γ). Strain alignment of the upper bainite part of the matrix near the wear surface.